frontiers in Earth Science

TYPE Original Research
PUBLISHED 09 March 2026
DOI 10.3389/feart.2026.1702148

OPEN ACCESS

EDITED BY
Raj Sunil Kandregula,
Pukyong National University,
Republic of Korea

REVIEWED BY
Tejpal Singh,
Council of Scientific and Industrial Research (CSIR), India
Vasiliki Mouslopoulou,
National Observatory of Athens, Greece

*CORRESPONDENCE
Marella Parnas,
marella.parnas@phd.unipi.it

RECEIVED 09 September 2025
REVISED 27 January 2026
ACCEPTED 29 January 2026
PUBLISHED 09 March 2026

CITATION
Parnas M, Viltres R, Pagli C, Keir D, La Rosa A and McNeill L (2026) New InSAR and seismology analysis of the 1995 Aigion M_w 6.2 earthquake (Greece). *Front. Earth Sci.* 14:1702148. doi: 10.3389/feart.2026.1702148

New InSAR and seismology analysis of the 1995 Aigion M_w 6.2 earthquake (Greece)

Marella Parnas[1]*, Renier Viltres [2], Carolina Pagli[1], Derek Keir[3,4], Alessandro La Rosa[1] and Lisa McNeill [3]

[1]Department of Earth Sciences, University of Pisa, Pisa, Italy, [2]National Center for Scientific Research, Earth and Environment Institute of Strasbourg, University of Strasbourg, Strasbourg, France, [3]School of Ocean and Earth Science, University of Southampton, Southampton, United Kingdom, [4]Department of Earth Sciences, University of Florence, Florence, Italy

As early rifts initiate and evolve, different fault geometries and kinematics may form. In particular, it is debated at what stage low–angle normal faulting can develop in continental rifts. Addressing this debate requires a thorough exploration of the variability and uncertainties of fault models derived from geophysical observations in order to constrain how faults slip during earthquakes. In addition, assigning earthquakes to particular faults is important for future hazard assessment. We study the M_w 6.2 Aigion earthquake that occurred in the Corinth Rift, Greece on 15 June 1995, using InSAR and seismic waveforms. Corinth is a rift in its early stages, currently extending at a rate of up to 15–20 mm yr^{-1} in the N-S direction and characterized by normal faults defining a graben. The Corinth Rift has experienced major destructive earthquakes and is densely populated. Still, the subsurface geometry, orientation, dip angle and location of the fault source of major earthquakes in the area, particularly the 1995 earthquake, is debated. We compute both ascending and descending co-seismic interferograms of the Aigion earthquake, which show up to 25.2 cm of ground motion away from the satellite (i.e., subsidence) on the north coast of the Gulf, with more deformation likely to have occurred offshore. We invert the interferograms for the best-fit fault model exploring the full range of fault parameters that explain the data. The modelling of only the InSAR data shows that either a north-dipping (39°) or south-dipping (45°) normal fault, striking roughly E-W, fit the data equally well. However, joint inversion of InSAR and teleseismic data favours a south-dipping fault (43°), in contradiction to the fault geometry interpreted so far in the literature. The use of multidisciplinary methodology to obtain robust fault models could better constrain subsurface definition of faults, both for past and future deformation events.

KEYWORDS
Aigion, Corinth, earthquake, InSAR, rift, teleseismic

1 Introduction

On 15 June 1995, a M_w 6.2 earthquake known as the Aigion earthquake occurred in the Gulf of Corinth (Greece), followed by an aftershock of M_w 5.2 (Bernard et al., 1997), also reported as M_w 5.6 by Lekidis et al. (1999) and M_s 5.4 by Lekkas et al. (1998). According to diverse sources, the earthquake caused 26 deaths, 200 injured and thousands of homeless and displaced people (Athanasopoulou, et al., 2008; Lekidis et al., 1999). Damage occurred in the cities of Aigion, Eratini and Valimitika, where

TABLE 1 Comparison of fault solutions for the Aigion earthquake. Including this study, **Bernard et al. (1997)** fault projection at the surface and epicentre (centre of the fault plane in depth), NEIC: National Earthquake Information Center, GCMT: Global Centroid Moment Tensor, ISC: International Seismological Centre, NOA: National Observatory of Athens.

Author	Lat (°)	Lon (°)	Mw	Ms	Depth (km)	Strike (°)	Dip (°)	Rake (°)
Bernard et al., 1997 surface projection	38.28	22.22		6.2	10	275	33	−83
Bernard et al., 1997 epicentre	38.35	22.2						
NEIC	38.40	22.28	6.5	6.5	14.2	276	34	−73
GCMT	38.10	22.46	6.5	6.5	15	265 102	43 48	−103 −78
ISC	38.39	22.27		6.4	26.1			
NOA	38.37	22.15	5.6		26			
Makropoulos et al. (2012)	38.40	22.27	6.3	6.5	3			
This study	38.28	22.24	6.2		5.89	97	43.2	

apartment buildings and hotels collapsed, with total economic loss reaching up to 600 million USD (NOAA database). The event was felt over a 225 km radius from the epicentre (USGS).

Despite the Aigion earthquake being amongst the largest shallow earthquakes in Europe in the last 50 years, there is still significant debate about the position and geometry of the source fault. Table 1 describes the different fault parameters interpreted for the June 15th M_w 6.2 Aigion earthquake by various agencies and publications. These show variations in the location and depth of the earthquake. The majority of the regional and global earthquake catalogs locate the hypocentre at 14–26 km depth below the northern onshore margin of the Gulf of Corinth (Table 1). In contrast Bernard et al. (1997) located the hypocentre at 10 km depth roughly in the middle of the Gulf of Corinth (Figure 1; Table 1). The moment tensor of the mainshock is a normal fault, with the two nodal planes striking near east-west (Bernard et al., 1997). However, the non-unique nature of the seismically-derived moment tensor makes interpreting the actual fault plane difficult. To address this, Bernard et al. (1997) used inverse modelling of sparse onshore Global Navigation Satellite System (GNSS) data and one descending interferogram. They demonstrated that the observed ground motions and earthquake magnitude could be explained by a fault dipping 35° northwards, whose surface projection aligned with the eastern tip of the Aigion fault on the southern coast. The authors acknowledge that a south-dipping fault model provides a good fit to the InSAR, but they state that the GNSS motions and hypocentre locations are not compatible with a south-dipping fault, yet they do not show the fit of this model to the GNSS. Also, the hypocentre locations have uncertainties, and they have been located differently by the global catalogues (Table 1).

Extensional fault systems, including the Corinth Rift, present normal faults in a geometric configuration suitable for slip transfer from one fault to another (Peacock and Sanderson, 1994). This is demonstrated by several examples of M > 6 earthquakes (Mouslopoulou et al., 2022). The Tyrnavos earthquake sequence in 2021, for example, sequentially ruptured, over a period of 10 days, previously undetected faults through three (M_w 5.7–6.3) mainshocks (NOA). After digital fault mapping and kinematic modelling, the ruptures were attributed to a previously unknown relay structure. The faults have subtle geomorphology, with some being interconnected at depth (Mouslopoulou et al., 2022). In the Corinth Rift, including the western rift (the focus of this paper), offshore fault mapping (e.g., Nixon et al., 2024) demonstrates that multiple faults across and along the rift are active, increasing the possibility of multi fault rupture. This is also shown by the interactive map of AFG database (Begg et al., 2025).

The fault responsible for the Aigion earthquake raised questions concerning 1- the possibility of low-angle dipping faults accommodating the extension in an early-stage rift, 2- methodologies to overcome the complexity of monitoring offshore deformation and thus 3- the uncertainties associated with a fault model. This paper's aim is to use all the available geodetic and seismic data from the Aigion earthquake to accurately constrain the fault that slipped. To determine the fault parameters, we first invert the Interferometric Synthetic Aperture Radar (InSAR) data, and then we proceed to a joint inversion of InSAR data and teleseismic waveforms.

2 Tectonic setting and earthquake activity

The Gulf of Corinth is located in continental Greece. This region is an extensional province, influenced by the westward motion of Anatolia and south-westward motion of the southern Aegean, relative to Eurasia (Mckenzie, 1972; Mckenzie, 1978; Pichon and Angelier, 1979; Taymaz et al., 1990; Taymaz et al., 1991; Armijo et al., 1996; Taymaz et al., 2004; Taymaz et al., 2004). The westward motion is partly accommodated by the North Anatolian strike-slip fault system, which has been rotating counterclockwise since the Miocene (Yolsal-Çevikbilen et al., 2014), and branches westward, raising hypotheses of a connection with the Hellenic Trough (Taylor et al., 2011). The south motion is also associated with the rollback of the subducting slab of the African plate since the Late Pliocene (~2–3 Ma) and is accommodated by shortening in the Hellenic Trough (Mouslopoulou et al., 2025).

The Corinth Rift, which initiated around 5 Ma (e.g., Beckers et al., 2015; Bell et al., 2018), has not yet reached

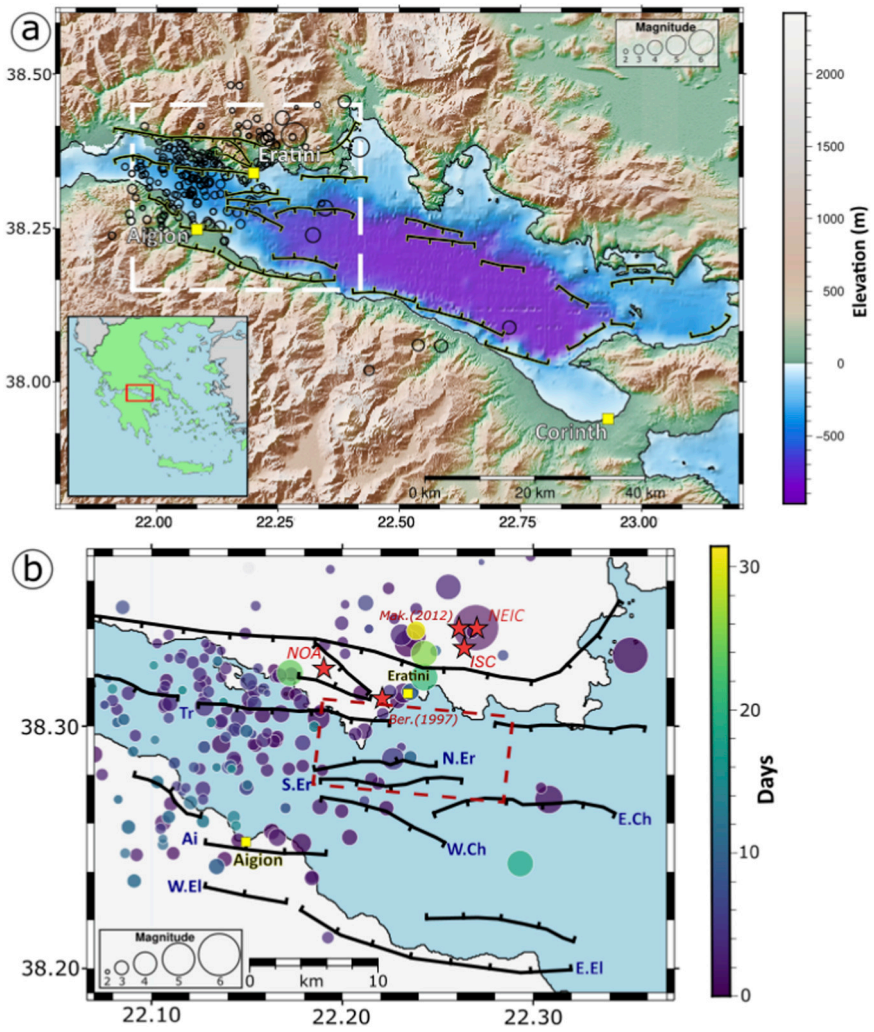

FIGURE 1
(a) Elevation map of the Gulf of Corinth with the seismicity from USGS catalogue from June 15th to 15 July 1995 (black circles) with inset showing the position of the Gulf in Greece by a red box; and **(b)** western part of the Corinth Gulf **(b)**. Red stars represent the epicentre locations of the 15 June 1995 Aigion earthquake reported by various monitoring institutions and in the literature such as Bernard et al. (1997); Makropoulos et al. (2012); NEIC: National Earthquake Information Centre; NOA: National Observatory of Athens and ISC: International Seismological Centre. Surface projection of the fault model by Bernard et al. (1997) is shown by the red dashed rectangle. The aftershocks are those reported for a month after the main event from USGS catalogue. The black segmented lines show the main faults (from Bell et al., 2008; McNeill et al., 2005a; Begg et al., 2025). Ai: Aigion fault; Tr: Trizonia fault; N.Er: North Eratini fault: S.Er: South Eratini fault; W.Ch: West Channel fault; E.Ch: East Channel fault; W.El: West Eliki fault; E.El: East Eliki fault. Yellow squares represent the location of the following cities: Corinth, Aigion, and Eratini.

continental breakup and is magma-poor. The N-S extension is thought to be mostly caused by major high-angle normal faults, striking E-W, from the Pliocene to Quaternary (Nixon et al., 2024; Taylor et al., 2011; Taymaz et al., 2007), although there is continued discussion about the role of low angle detachment faulting (Bell et al., 2018). This results in a rift measuring between 100 and 130 km in length, orientated in an east-west direction, and with a width of ~50 km (e.g., Koukouvelas and Doutsos et al., 1996; Bell et al., 2018). The topography of the southern margin is indicative of uplift in fault footwalls of the southern border fault system (up to 800–1000 m of relief), while the offshore basin is suggestive of continued subsidence and syn-rift sediment fill (see, for example, Nixon et al., 2024).

2.1 Active faulting within the western Corinth Rift

The principal normal faults of the rift are typically 10–20 km long, which have generated several subsidiary half-grabens across the rift (e.g., Koukouvelas and Doutsos et al., 1996; Bell et al., 2008). Major fault systems relevant to this study, such as the Eratini and Trizonia fault systems, as well as their overall orientations, are illustrated in Figure 1. Various seismic-reflection campaigns have been conducted in the western Gulf using marine multichannel seismic (MCS) surveys (e.g., Taylor et al., 2011; Bell et al., 2008; McNeill et al., 2005a), and shallow-penetrating grids of MCS offshore Aigion (McNeill et al., 2007) and in the Trizonia Basin

area (Beckers et al., 2015; Bernard et al., 2004). These datasets have enabled detailed mapping of offshore and coastal normal faults and characterization of the shallow tectonic architecture of the western rift basin (e.g., McNeill et al., 2005a; Bell et al., 2008; Jolivet et al., 2010; Nixon et al., 2016; Beckers et al., 2015). Reconstruction of the fault activity indicates that different segments of the rift evolved independently, reflecting spatial and temporal variations in extensional deformation, followed by fault linkage and contemporaneous development of deformation (e.g., Bell et al., 2008; Nixon et al., 2016).

The slip rates of the major normal faults (e.g., McNeill et al., 2005b; Bell et al., 2008; Bell et al., 2009; Nixon et al., 2024) demonstrate that in the western rift much of the deformation today is along the southern shore on the border fault system which appears to be kinematically linked (Nixon et al., 2024), but that other active faults offshore have significant slip. The principal mapped faults in the study area, onshore and offshore, include the Aigion fault (3.5–11 mm yr^{-1}), the West and East Eliki faults (2.0–11.0 mm yr^{-1}) along the southern coast, as well as offshore structures such as the West Channel fault (~0.4–0.5 mm yr^{-1}), the East Channel fault (up to ~1.2 mm yr^{-1}), the North Eratini fault (2.0–6.7 mm yr^{-1}), and the South Eratini fault (~1.4 mm yr^{-1}) (Figure 1; slip rates from De Martini et al., 2004; McNeill et al., 2005a; Bell et al., 2008; Beckers et al., 2015; Nixon et al., 2024). Note that slip rate ranges given here in many cases come from multiple studies and methodologies and encompass the full published ranges.

The high level of fault activity results in a fast-deforming region, producing numerous large-magnitude earthquakes, including the 373 BC Elike earthquake (Stiros, 2021; Clément et al., 2004), the 1746 and 1817 earthquakes which destroyed the city of Aigion (Stravropoulos, 1954), the 1861 Ms ~7 Eastern Eliki fault rupture (Schmidt, 1879; Clément et al., 2004; McNeill et al., 2005b). In addition, east of the study area, the 1981 eastern sequence of the Alkyonides Gulf with multi-earthquake and multi-fault rupture of both north- and south-dipping faults (Ms 6.7, 6.4, 6.4; Jackson et al., 1982; Taymaz et al., 1991).

Alongside these major events, the western rift exhibits persistent seismic activity expressed as prolonged micro-seismic sequences and swarms. Several long-term seismic episodes can be cited, such as the 2003–2004 offshore seismic crisis north of Aigion, which was interpreted as associated with a hydroshear process (Duverger et al., 2015), the 2003–2004 fluid-induced seismic crisis (De Barros et al., 2020), the six-month-long 2010 Efpalio sequence, which affected much of the western Gulf up to Trizonia Island (Sokos et al., 2012), the 2013 swarm 4 km southeast of Aigion on a 50° north-dipping surface (Kapetanidis et al., 2015), and the Marathias seismic sequences from 2020 to 2021, associated with normal faulting, as evidenced by Kaviris et al. (2021). Paleoseismological trenching studies in the western rift (e.g., Koukouvelas et al., 2001; McNeill et al., 2005; Palyvos et al., 2005) and in the eastern rift (Collier et al., 1998) suggest recurrence intervals of ~200–600 years on the primary, high slip rate southern border faults.

2.2 Extension rates (GNSS) and seismicity

The Corinth Rift is amongst Europe's most seismically active regions. The GNSS measurements in the rift show that the extension rate varies from 5–10 mm yr^{-1} in the east (Briole et al., 2000; Clarke et al., 1998) to 15–20 mm yr^{-1} in the west (Avallone et al., 2004; Briole et al., 2000). Despite being relatively immature, the Corinth Rift is one of the fastest extending continental rifts (e.g., East African rift system 2 mm yr^{-1} (Saria et al., 2014) for ca. 32 Ma (Omar and Steckler, 1996), Baikal rift with 4–5 mm yr^{-1} (Calais et al., 1998) since ca. 3 Ma (Mats, 1993)). The along-rift variations in extension rate may account for the marked increase in the amount of microseismicity in the west (Bell et al., 2018). Since 2000, levels of seismicity (mostly M1–4) have been highest in the west (Lambotte et al., 2014; Duverger et al., 2018). High-resolution images of the microseismicity at depth have been used to make a link between day-to month-long earthquake swarms and potential specific tectonic structures (Duverger et al., 2015). The seismicity is not homogeneous across the Gulf (Bell et al., 2008; Lambotte et al., 2014). Our zone of interest shows a few small earthquake clusters under the northern coast at 10–15 km depth, but these sequences do not highlight distinct fault planes in depth. In addition, there is a lack of earthquakes around the North Eratini fault offshore (fault details in McNeill et al., 2005a; Bell et al., 2008; see also Duverger et al., 2018). The Aigion area itself seems to mark a change in earthquake activity betwen regions to its west and east (Lambotte et al., 2014). To the west, microseismicity is common, with a dominant feature being the clustering of earthquakes at 6–10 km depth in a relatively low-angle zone dipping north, interpreted by some as fluid induced earthquakes along a detachment fault (Rigo et al., 1996; Lyon-Caen et al., 2004) or the base of the brittle crust (Hatzfeld et al., 2000). It has been demonstrated that the integration of remote sensing techniques with geological methods can enhance the retrieval of subsurface geometry (Singh et al., 2025). Furthermore, it has been observed that fault structures above this zone of microseismicity dip at much higher angles (e.g., Bell et al., 2008; Bell et al., 2018). In contrast, less microseismicity is observed in the Central part of the rift, east of Aigion (Duverger et al., 2018). In addition, new evidence from focal mechanisms has shown that the shallow microseismicity in the Gulf of Corinth is associated with east-west normal faulting, which contrasts with the deeper microseismicity with strike-slip mechanisms in the Gulf of Patras to the west (Nikolopoulou et al., 2025).

3 Data and methods

To determine the source geometry and location of the 1995 Aigion earthquake, we have used both InSAR data and seismic waveform recordings. We have produced both ascending and descending Line-of-Sight (LOS) interferograms using images acquired by ERS1 (European Remote Sensing Satellite, C-band) to measure the deformation and inverted them for the fault source parameters. We then use both the InSAR data and the seismic waveforms of the earthquake recorded at regional to teleseismic distances to perform a joint inversion for the earthquake and fault source parameters.

3.1 InSAR processing and modelling

Interferometric synthetic aperture radar (InSAR) has been used to measure different types of surface displacement since the 1990s. The earliest applications included to measure ice sheet motion in Goldstein et al. (1993), and for co-seismic slip of the M_w 7.3 Landers in 1992 by Massonnet et al. (1993). The technique is now also routinely used to measure magma motions at volcanoes (e.g., Sigmundsson, 2018) and for longer term tectonic plate boundary motion velocities from which strain rates can be derived (e.g., Wright et al., 2023). The main difference between past and recent missions is the number of acquisitions and the revisit time of the satellites over a study area. Past European SAR missions did not systematically acquire images over a given area and at best, the shortest revisit time was about 1-month (Ferretti et al., 2007) while recent missions guarantee continuous acquisitions over all actively deforming zones globally at revisit times as short as a few days. This has resulted in a major step change in our capability of deriving average velocity maps with accuracy of only a few mm's and times-series of rapidly evolving displacements. But, using old or new SAR data to study a sudden event, like an earthquake, is not significantly different. The ERS1 data, ascending and descending, were processed using the software package InSAR Scientific Computing Environment (ISCE2) (Rosen et al., 2012; Vaka et al., 2020). For the processing, Single Look Complex (SLC) acquisitions were first co-registered using the precise ERS orbits files (DOR) and a 3 arc-seconds (90 m) Shuttle Radar Topography Mission (SRTM) Digital Elevation Model (DEM, Farr et al., 2007). The interferograms were then filtered using the Goldstein adaptive power spectral filter (Goldstein and Werner, 1998) with a standard strength of 0.5 and then unwrapped using the ICU branch cut algorithm (Goldstein et al., 1988). Finally, the interferograms were geocoded using the 90 m SRTM DEM. Phase unwrapping errors were fixed manually, or masked (if of small extension), before the modelling. Using different viewing geometries gives more robust constraints on the vertical and E-W components of motion. The ascending co-seismic interferogram (track 415) spans a 3-month period (April 13th–18 July 1995) and the descending co-seismic interferogram (track 279) spans a similar time period (April 29th–9 July 1995) (Figure 2), allowing joint inversion of the two ascending and descending interferograms. Both ascending and descending interferograms show the same deformation pattern on the north coast of the Corinth Gulf, indicating the dominant part of the surface displacement was vertical. On the wrapped descending interferogram, ~9 fringes are visible on the north coast, west to Eratini, resulting in an onshore visible minimum displacement of 25.2 cm (a fringe is 2.8 cm) (Supplementary Figure S1). However, the fringe pattern is truncated by the coastline indicating that the majority of the subsidence likely occurred offshore. The south side of the Gulf shows no clear fringe, indicating negligible ground motion.

We used the quadtree-partitioning algorithm to reduce the data size of the interferograms while keeping the significant displacement information. Using this algorithm, the interferogram is divided into four quadrants and the mean of each quadrant is calculated, then the root mean square (RMS) scatter is calculated for each quadrant (Supplementary Figure S1). If the RMS scatter is above a set threshold of 8.5 mm, the quadrants are divided into four until converging (Jónsson et al., 2002; Welstead, 1999). From this process, the number of data points where the deformation gradient is high is represented in a denser way compared to the rest of the interferogram and the number of total data points and noise is diminished (Supplementary Figure S2).

We inverted the InSAR data combining a Monte Carlo simulated annealing algorithm and a derivative-based algorithm, to reach the real minimum of the misfit function, which is the cost function optimized to find the global minimum (Cervelli et al., 2001). We explained the signal assuming a single Okada rectangular shear dislocation source (Okada, 1985) buried in an elastic half-space with Poisson's ratio of 0.25 and shear modulus of 30 GPa. We let the fault location, strike and dip vary freely but the remaining fault parameters were more tightly constrained between a-priori values according to observations collected in the region (Table 2). We also assumed the fault has no strike-slip component. The modelling parameters of each model are detailed in Table 2. Additionally, the error bar on the best-fit source parameters was calculated with a Monte Carlo simulation of correlated random noise (Wang et al., 2014). We construct 100 simulations of spatially correlated random noise based on the variance-covariance matrix for each interferogram. These noise simulations are then added to the original interferograms and inverted 100 times. Hence, we obtain 100 different model solutions, and the uncertainties of each source parameter can be estimated from the 90% confidence interval of the solutions (see Figures 5, 6).

3.2 Joint inversion of InSAR and teleseismic data

The InSAR data are analysed using the PSGRN and PSCMP Fortran packages to calculate deformation in an elastic half space during co- and post-seismic stages (Wang et al., 2006). The first package calculates for various depth dislocation sources, their time dependent Green's function and associated primary parameters (strike–slip double–couple, the dip–slip double–couple, the compensated linear vertical dipole and the point inflation), while the second package modelized and discretize diverse deformation pattern over a wide rupture area (Wang et al., 2006). Here Green's functions are calculated for a depth-distance range of 10 km with 1 km spacing in both vertical and horizontal directions. In addition, the offset and orbital ramp components are added to the InSAR data. The re-estimation of the complete geodetic data and the source fault parameters permit the use of derived covariance matrices for data weighting in the down sampling. The down sampling is based on statistically significant fractions depending on the 2D quantization algorithm (Jónsson et al., 2002).

3.2.1 Data and station choice

The event was large enough to be recorded by the global seismic network. The waveforms were download from the FDSN service (International Federation of Digital Seismograph Networks) for the event time on 15 June 1995, at 00:15 (UTC). The stations were selected depending on their signal-to-noise ratio and to

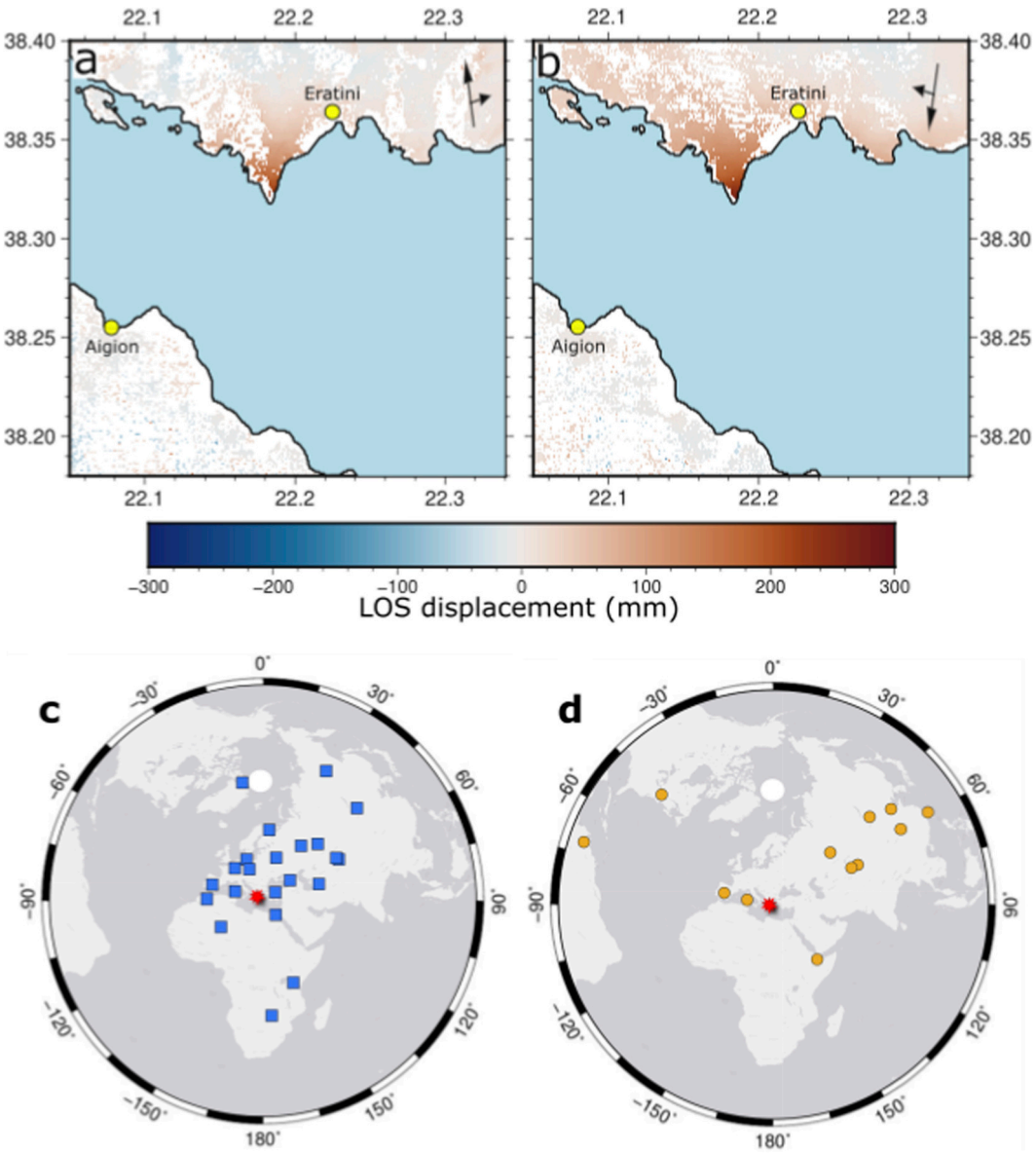

FIGURE 2
Top panel, **(a)** ascending and **(b)** descending unwrapped interferogram from ERS-1 satellite. In top right corners, long arrow shows the satellite flight direction, short arrow shows Line-of-Sight (LOS) displacement. Bottom panel, **(c)** location of the seismic stations providing P and **(d)** S waves. In blue squares, seismic stations used for P waves. In orange circles, seismic stations used for S waves.

TABLE 2 **Parameters range for InSAR inversion.**

	Lon (°)	Lat (°)	Dip (°)	Depth (km)	Length (km)	Width (km)	Dip-slip (m)
Parameters range	22.10–22.28	38.20–38.34	0–90	0–12	5–18	1–10	-2–0

achieve good azimuthal coverage (Figure 2). We avoid using stations too close or too far from the event to ensure reduced noise issues but maintain sufficient signal strength, keeping in mind that the seismic network in 1995 was less dense then today. We used 19 stations for P and 11 for S waveforms listed in Supplementary Figure S3.

3.2.2 Waveforms treatment

For seismogram processing, we restored the true ground displacement by rotating it into radial, transverse and vertical components. Then, waveforms are shifted according to a bandpass-filter from 100 s to 20 s to buffer the effects of high-

frequence noise (Steinberg et al., 2020) which induce phase shifts. The vertical (Z) and transverse (T) components were used respectively to fit the P and SH waveform, for a time window of 20 s before and 35 s after wave arrivals.

Seismic data are then assessed through the QSSP package which uses calculated Green's function specific to those data with 1 km spacing grid laterally and 1 km vertically for a depth range of 60 km. Moreover, time shifts specific to each station are estimated during the optimization to account for velocity model errors (Mustać et al., 2020; Vasyura-Bathke et al., 2020; Viltres et al., 2021). Green's functions defining the model of wave propagation on a distance-depth grid are used for the creation of synthetic seismogram data for any given source-receiver couple at different depths and locations (see Supplementary Figure S3).

3.2.3 Joint inversion

Once compiled, the interferograms and seismic waveforms are simulated through two velocity and structural models. The elastic property of the AK135 high-resolution model, is used for the mantle and core structure (Kennett et al., 1995); and the water layer of the Gulf is removed and replaced by the global velocity model CRUST2, a 3-D model for crustal velocity, density and thickness (Bassin, 2000).

Finally, we proceed to the inversion using the Bayesian Earthquake Analysis Tool (BEAT; Vasyura-Bathke et al., 2019; Vasyura-Bathke et al., 2020), an open-source software using the Bayesian theorem (Bayes, 1763) to retrieve source parameters based on joint inversion of seismic waveforms and geodetic data from InSAR. In the function used, the variable d_k^{obs} expresses a dataset k which is either a seismic waveform component at a station, or a displacement field of an unwrapped interferogram in LOS. With the following assumption of Gaussian distributed residuals $r_k(m) = d_k^{obs} - d_k(m)$, where $d_k(m)$ is the predicted synthetic data for the dataset k; and the posterior probability density of model parameters m for the datasets is given by the equation:

$$p\left(m\middle|d^{obs}\right) \propto p(m)\Pi_{k=1}^{k} \frac{1}{\left(2\pi\sigma_k^2\right)^{N/2} C_k^{1/2}} \exp\left[-\frac{1}{2\sigma_k^2}[r_k(m)]^T C_k^{-1}[r_k(m)]\right]$$

The covariance matrix C_k for the noise statistics of residual errors that are considered noise. Hierarchical scaling σ_k is used to estimate the standard deviation of the residuals. Then, we sample the posterior probability density using a Monte Carlo algorithm (Del Moral et al., 2006; Vasyura-Bathke et al., 2020), an adaptive version of Markov Chain Monte Carlo sampling.

4 Results

4.1 InSAR inversion results

The model of the interferograms can be fit equally well by a north-dipping fault or a south-dipping fault, both positioned mainly offshore. The best-fit parameters obtained for each model are presented in Table 3.

The north-dipping solution (Figure 3) consists of an offshore normal fault striking $269°^{+4.2}_{-0.1}$, with a medium dip angle, $39°N^{+0.3}_{-2.8}$. This rupture plane is mostly beneath the Gulf and relatively shallow, with the top of the fault at 4.0 ± 0.5 km depth. At depth it extends below the north coast. The surface projection of the fault appears to be offshore as well and would correspond to the east continuity of the Aigion fault. The geodetic magnitude of this model is a M_w 6.2 in agreement with the seismic solution (Table 1). The RMS misfit is 10 mm.

Furthermore, we also allowed the inversion to explore solutions of south-dipping faults (Figure 4), and we found a south-dipping best-fit model that fits the data as well (RMS misfit of 10 mm) as the north-dipping solution. This fault plane is entirely offshore and is oriented east-west, strike 91° ± 0.5, 45°S ± 1.5. The surface projection of the fault is onshore, through Tolofona city. The geodetic magnitude of this model is also M_w 6.2.

For both solutions, the confidence intervals are on the order of 10^{-2} to 10^{-3} and well constrained for each parameter (see Figures 5, 6) and the full deformation pattern can be recovered (Figure 7).

4.2 Joint inversion results

The best-fit model obtained by the inversion of both seismic and InSAR data is shown in Figure 8. Like the previous results, it retrieves a magnitude of M_w 6.2. The strike direction is $97°^{+0.74}_{-0.64}$ and the intermediate dip angle is 43° towards the south. In this solution, the fault is $12.33^{+0.6}_{-0.04}$ km long and 6.5 $km \pm 0.02$ wide, with a depth of 5.8 $km \pm 0.06$. The surface projection of the fault partly onshore on the west and offshore to the east following the north coastline. The slip is 1.5 m ± 0.01, for a near vertical rake of −103° ± 0.1. The fault parameters for the joint inversion solution are presented in Figure 9 and demonstrate a well-constrained distribution.

To summarize, the inversion of the InSAR data only shows that the data is consistent with both a north- and south-dipping normal fault beneath the Corinth Rift. The fault that is modelled by the joint inversion of InSAR and the seismic waveforms has a similar position, strike, length and dip angle to the south-dipping fault modelled from the InSAR data only. The parameters of each solution are listed in Table 3.

5 Discussion

5.1 South-dipping fault preferred solution

The solutions from inversion of InSAR data show that both north- and south-dipping faults fit the data equally well with RMS misfit of 10 mm for both solutions.

The north-dipping solution is broadly similar to that interpreted by Bernard et al. (1997) with a similar strike (275°) and dip angle (35°) but with a larger fault rupture area. Consequently, the slip displacement of the Bernard et al. (1997) model is smaller than the one presented here, with 0.87 m compared to 1.4 m. Additionally, our fault projection to the surface is offshore and aligns with an eastward continuation of the Aigion fault. It is important to note that Bernard et al. (1997) state that the GPS data does not permit a south-dipping solution. Consequently, they did not

TABLE 3 Best fit fault parameters for the different solutions.

Model	Lon	Lat	Strike (°)	Dip (°)	Depth (km)	Length (km)	Width (km)	Slip (m)	Mw	RMS (mm)
North-dipping model	22.19	38.29	269	39.3	3.95	7.95	7.31	1.4	6.2	10
South-dipping model	22.20	38.31	91.2	44.9	6.04	7.93	3.1	2.9	6.2	10
InSAR and Seismology best-fit model	22.24	38.28	97	43.2	5.89	12.33	6.5	1.5	6.2	26.7

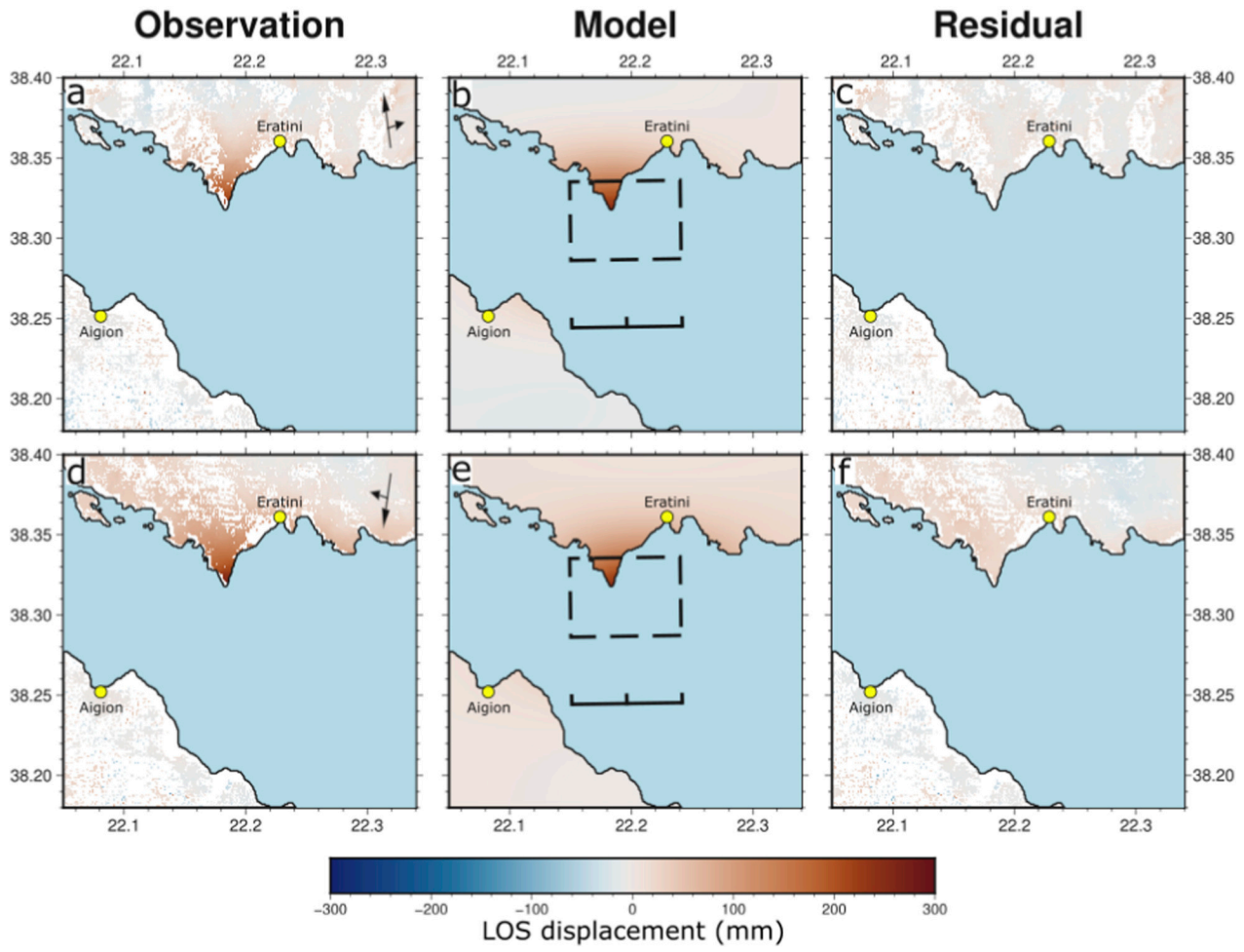

FIGURE 3
North-dipping fault solution retrieved with InSAR data. **(a)** Observation data in ascending view; **(b)** model in ascending view; **(c)** residual in ascending view; **(d)** observation data in descending view; **(e)** model in ascending view, **(f)** residual in descending view. The surface projection of the fault is represented by a black line. The rupture plane is shown by a dashed rectangle.

fully consider the feasibility of their south-dipping model and its implications.

The alternative InSAR solution in this study is a south-dipping fault plane with a dip angle of 45°. Notably, the slip of this solution is higher (3 m) to compensate for the smaller and deeper modelled rupture plane. Regarding the surface projection, it aligns, within about 400 m, with the Trizonia fault (Begg et al., 2025). The north- and south-dipping fault models both retrieve the observed M_w 6.2 magnitude, with the variation in fault geometry and slip amount within the range expected from the Wells and Coppersmith (1994) globally-derived empirical relationship between fault parameters and earthquake magnitude. So far, the inversion of InSAR data reveals two potential normal fault sources with moderate dip angle which could nucleate the M_w 6.2 earthquake and fit with the

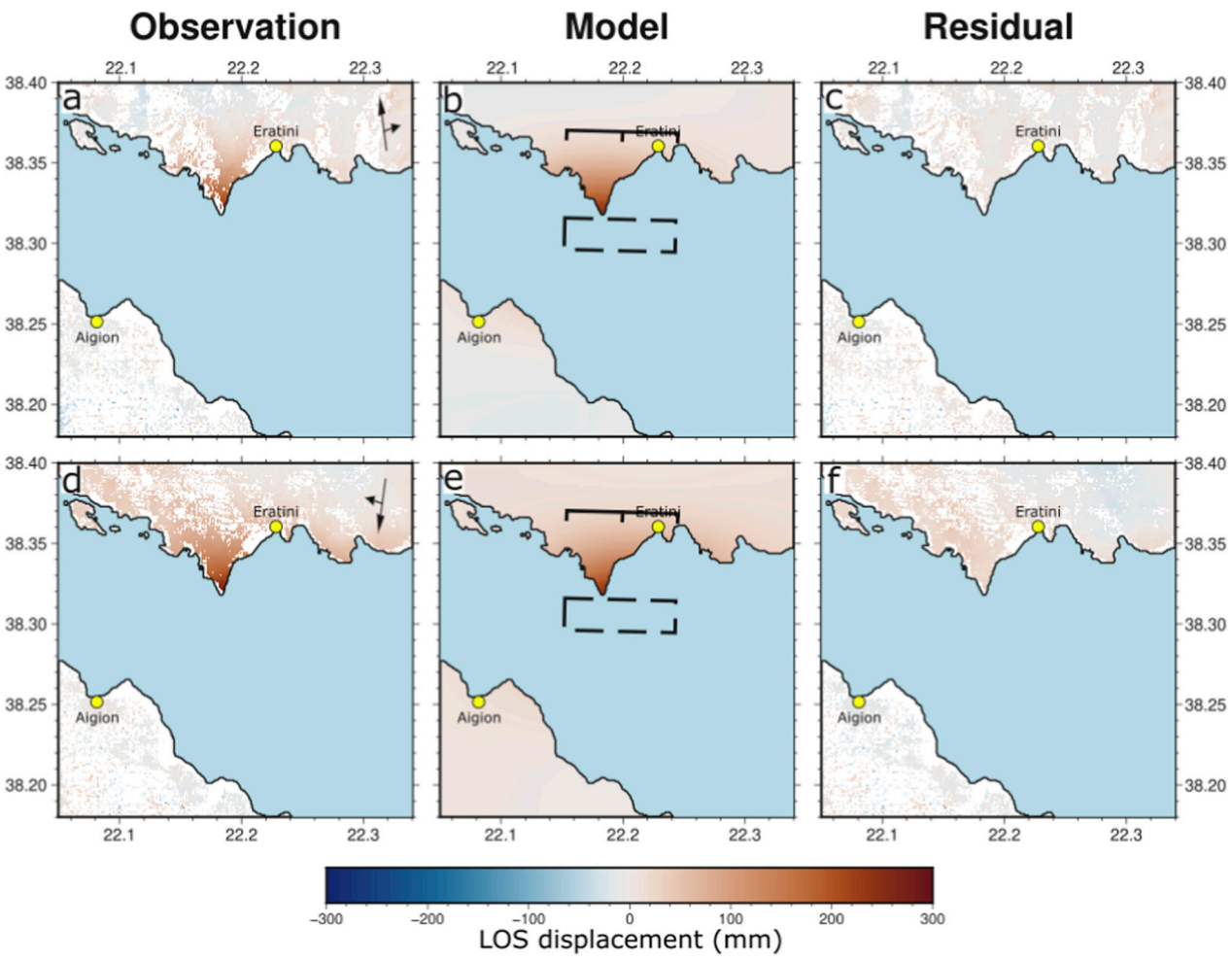

FIGURE 4
South-dipping fault solution retrieved with InSAR data. **(a)** Observation data in ascending view; **(b)** model in ascending view; **(c)** residual in ascending view; **(d)** observation data in descending view; **(e)** model in ascending view, **(f)** residual in descending view. The surface projection of the fault is represented by a black line. The rupture plane is shown by a dashed rectangle.

structure of the rift for fault geometry and location (see faults mapped on Figure 1b). Nevertheless, the inversion permits to reconstruct the full pattern of ground movement, showing an oval shape that is stretched out in an east-west direction (Figure 7). This shows that the main surface displacement is offshore and larger than that captured onshore in the original InSAR data. Also, we note that the observed interferograms do not show any uplift. In fact, for normal faults the component of footwall uplift during earthquakes tends to be significantly smaller than the hanging wall subsidence, thus this finding is not surprising (e.g., Stein and Barrientos, 1985; Stein, 1988). Those features heavily contribute to the non-uniqueness of the models. To choose a preferred orientation, the addition of the seismological inversion was necessary.

The joint inversion solution, combining geodetic and seismological datasets, suggests an east-west striking normal fault slightly longer (12 km) than the ones for the InSAR only inversion. Especially, this solution presents a moderate dip angle (43°) to the south. The solution shows a very narrow standard error and a well-shaped bell curve for the distribution of the diverse parameters. Combining the two datasets, we reach an acceptable RMS value of 27 mm. The modelled fault is broadly similar to the south-dipping solution retrieved from inversion of InSAR data only, except for the fault plane dimensions being larger and the fault position being further offshore. The fault length and slip are consistent with structural measurements of typical fault length in the Corinth Rift and the amount of slip observed in similarly sized earthquakes in the region. The length is similar to the typical 10–20 km fault segment length measured in both surface geology and from subsurface seismic reflection data (e.g., Koukouvelas and Doutsos, 1996; Bernard et al., 1997; Beckers et al., 2015; Bell et al., 2008). In addition, the modelled slip of 1.5 m is comparable to that measured for nearby large earthquakes such as the M_w 6.4 Lefkada earthquake on 17 November 2015, in which calculated fault slip from kinematic inversion was 1.5–1.6 m (Sokos et al., 2016; Melgar et al., 2017). Furthermore, examples of fault slip are the earthquakes of the 3rd, 4th and 12th of March 2021 in Thessaly, Central Greece, where the three major events were of magnitudes M_w 6.3, 6.2 and 5.7 with respective slips of 1.2–1.5 m, 1.2 m and 1.0 m (Papadopoulos et al., 2021).

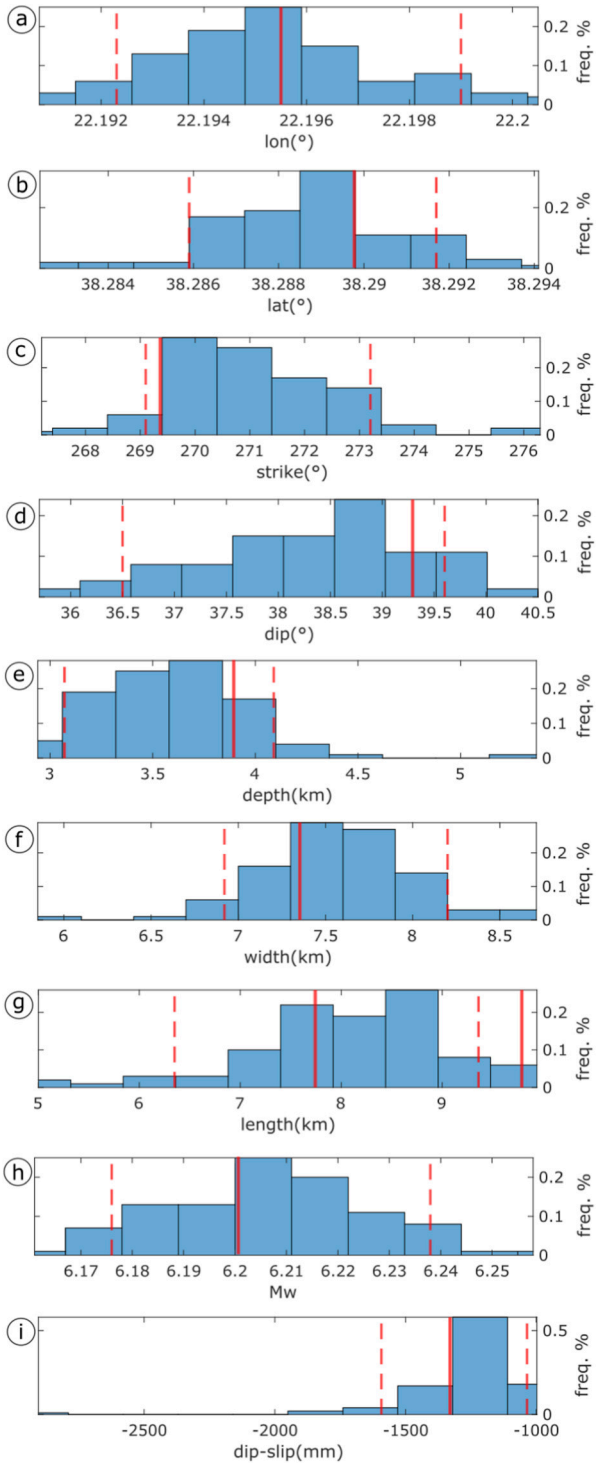

FIGURE 5
Distribution of the fault parameters for the north-dipping solutions obtain with InSAR inversion. **(a)** Longitude in degrees; **(b)** latitude in degrees; **(c)** strike in degrees; **(d)** dip angle in degrees; **(e)** depth in km; **(f)** width in km; **(g)** length in km; **(h)** Magnitude Mw; **(i)** dip slip in mm. Dashed red lines indicate the border of the 90% confidence interval; red lines indicate the value of the model.

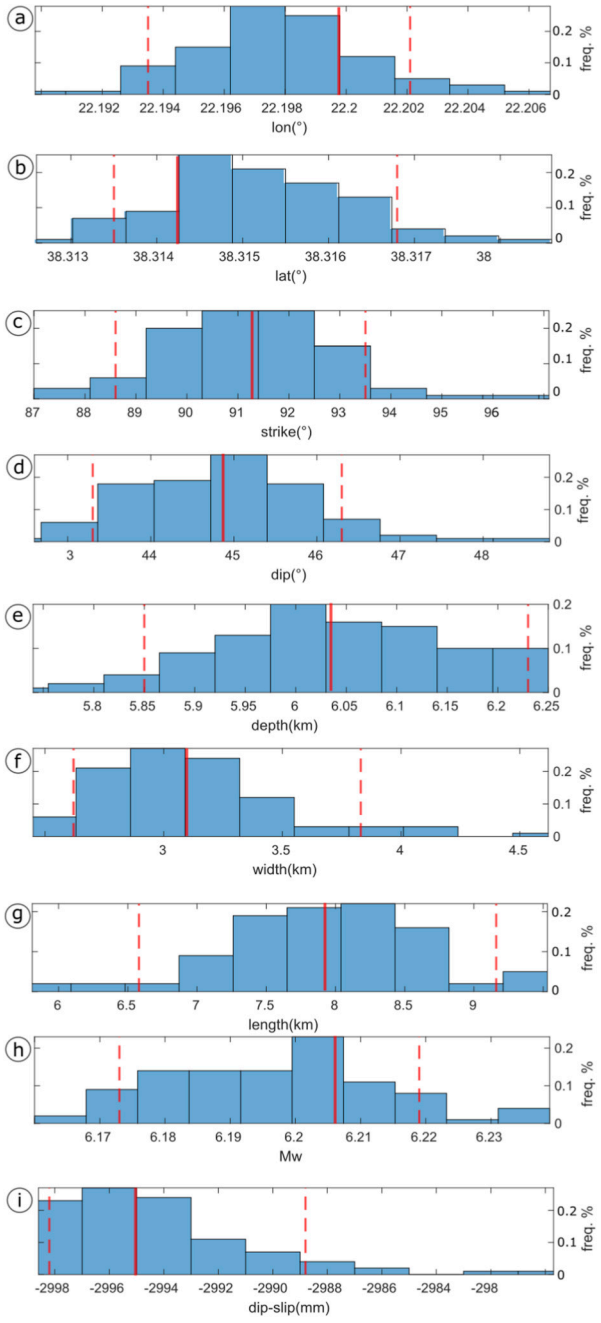

FIGURE 6
Distribution of the fault parameters for the south-dipping solution obtain with InSAR inversion. **(a)** Longitude in degrees; **(b)** latitude in degrees; **(c)** strike in degrees; **(d)** dip angle in degrees; **(e)** depth in km; **(f)** width in km; **(g)** length in km; **(h)** Magnitude Mw; **(i)** dip slip in mm. Dashed red lines indicate the border of the 90% confidence interval; red lines indicate the value of the model.

It is quite difficult to correlate the surface projection of the fault with mapped faults, whether onshore or offshore. One issue is that fault mapping is challenging in the nearshore areas

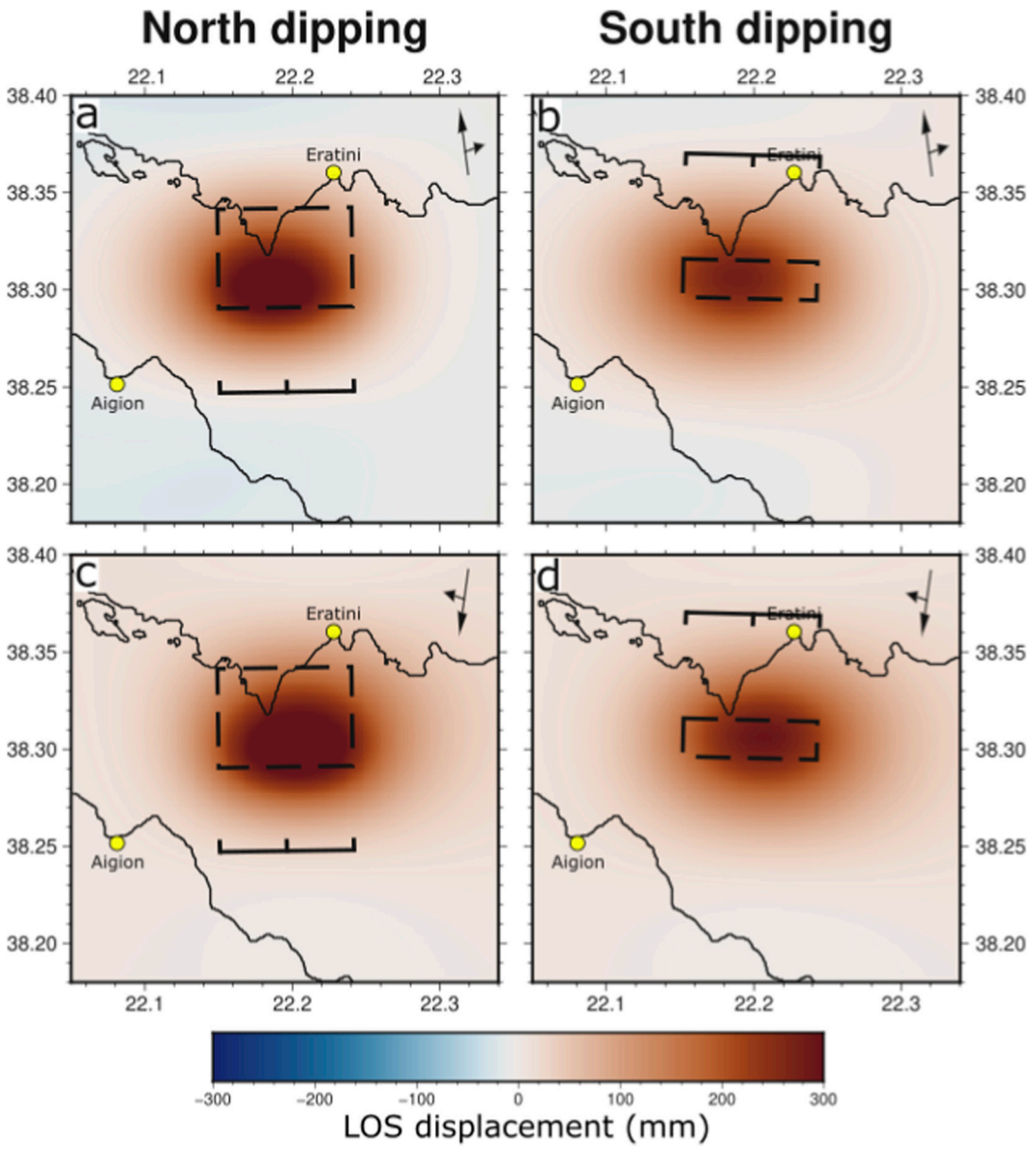

FIGURE 7
Reconstructed pattern of Line-of-Sight (LOS) displacement associated with the best fit models obtained from InSAR inversion, including that which is expected to have occurred offshore. **(a)** Model of the North-dipping deformation pattern in ascending view; **(b)** model of the south-dipping deformation pattern in ascending view; **(c)** model of the North-dipping deformation pattern in descending view; **(d)** model of the south-dipping deformation pattern in descending view.

where slopes are steep and sediments are coarse grained, resulting in poor seismic imaging and some faults therefore not being accurately mapped here. Secondly, there are few clear indicators of well-constrained Holocene uplift along the northern coast in the western rift (such as bedrock notches) to indicate an active fault, because the bedrock here is composed of more erodible lithologies (Bell, 2008). However, the surface projection of our joint inversion modelled fault is coherent and can fit with the Trizonia fault system mapped on- and offshore, along the north coast (Beckers et al., 2015; Begg et al., 2025). We therefore interpret that the source of the 1995 earthquake is possibly the eastward subsurface projection of the S-dipping Trizonia fault system, which is categorized as active (Begg et al., 2025). The lack of clear geological uplift on the northern coast can be explained by the presence of an active fault network with multiple sub-parallel faults that straddle the coastline, but also the rocky substrate, complicating the picture. In this scenario normal faults onshore cause subsidence of the coastline, while normal faults offshore cause uplift of the coastline.

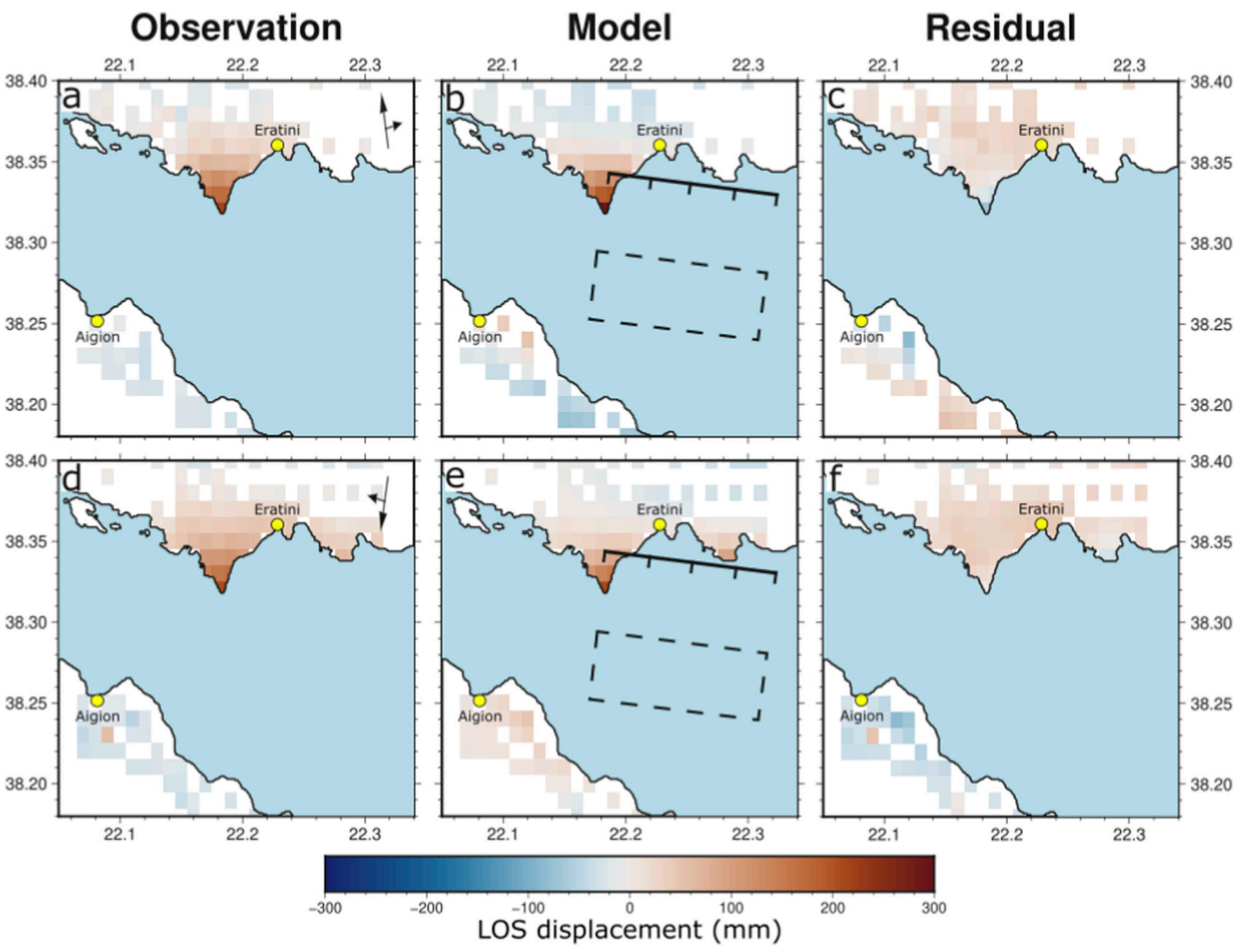

FIGURE 8
Joint inversion solution of InSAR and seismic data. **(a)** Observation data in ascending view; **(b)** model in ascending view; **(c)** residual in ascending view; **(d)** observation data in descending view; **(e)** model in ascending view, **(f)** residual in descending view. The surface projection of the fault is represented by a black line. The rupture plane is shown by a dashed rectangle.

5.2 Implications for rift structure, fault behaviour and earthquake hazards

For the location of the rupture, the models all agreed on a longitude band between 22.20° and 22.25° for the top centre of the fault rupture. In the Corinth rift, the Aigion region is also recognised as a transition zone in rift structure. It includes a bathymetry difference between the shallow (~400 m depth) westernmost part of the rift and the deeper (~900 m water depth) central part of the rift where there is widening of the Gulf from west to east (Bell et al., 2018; Cornet et al., 2004; Koukouvelas and Doutsos, 1996) (Figure 1a). The western rift is also composed of multiple N- and S-dipping active faults and distributed deformation (e.g., Begg et al., 2025; Bell et al., 2008; McNeill et al., 2005a), in contrast to further east. In this scenario normal faults onshore cause subsidence of the coastline, while normal faults offshore cause uplift of the coastline. The fault map on the north coast of the study region is consistent with this scenario (Figure 1b). Several major normal faults are mapped at the coasts and offshore, including the Trizonia fault, the Aigion fault, the Eratini faults and the West Channel fault system, which is consistent with this scenario (e.g., McNeill et al., 2005a; Bell et al., 2008; Beckers et al., 2015; Begg et al., 2025).

The rupture area described by our model is coherent with the description of coseismic damage. Lekkas et al. (1998) present an extensive study of the effects of the earthquake, detailing the damage on both the north and south coast. The extent of the damage zone is bigger on the south coast, 12 km by 3 km, while it is smaller, 1 km by 0.1 km, close to Eratini on the north coast. Also, the co-seismic surface cracks presented in Bernard et al. (1997) (i.e. 2 cm wide fractures striking N 105° and N 95°) cannot be associated with certainty to the main fault that ruptured (Lekkas et al., 1998; Koukouvelas and Doutsos, 1996). The ground fractures are also very small and also not observed in the InSAR data, with Lekkas et al. (1998) concluding that they likely formed because of ground shaking and not directly from fault slip. Another interpretation is that fractures could have opened during the mainshock and elongated during the aftershocks (Koukouvelas and Doutsos, 1996), though this is not supported by the InSAR observations. These studies also mentioned meter-scale coastline changes on both shores, causing landslides

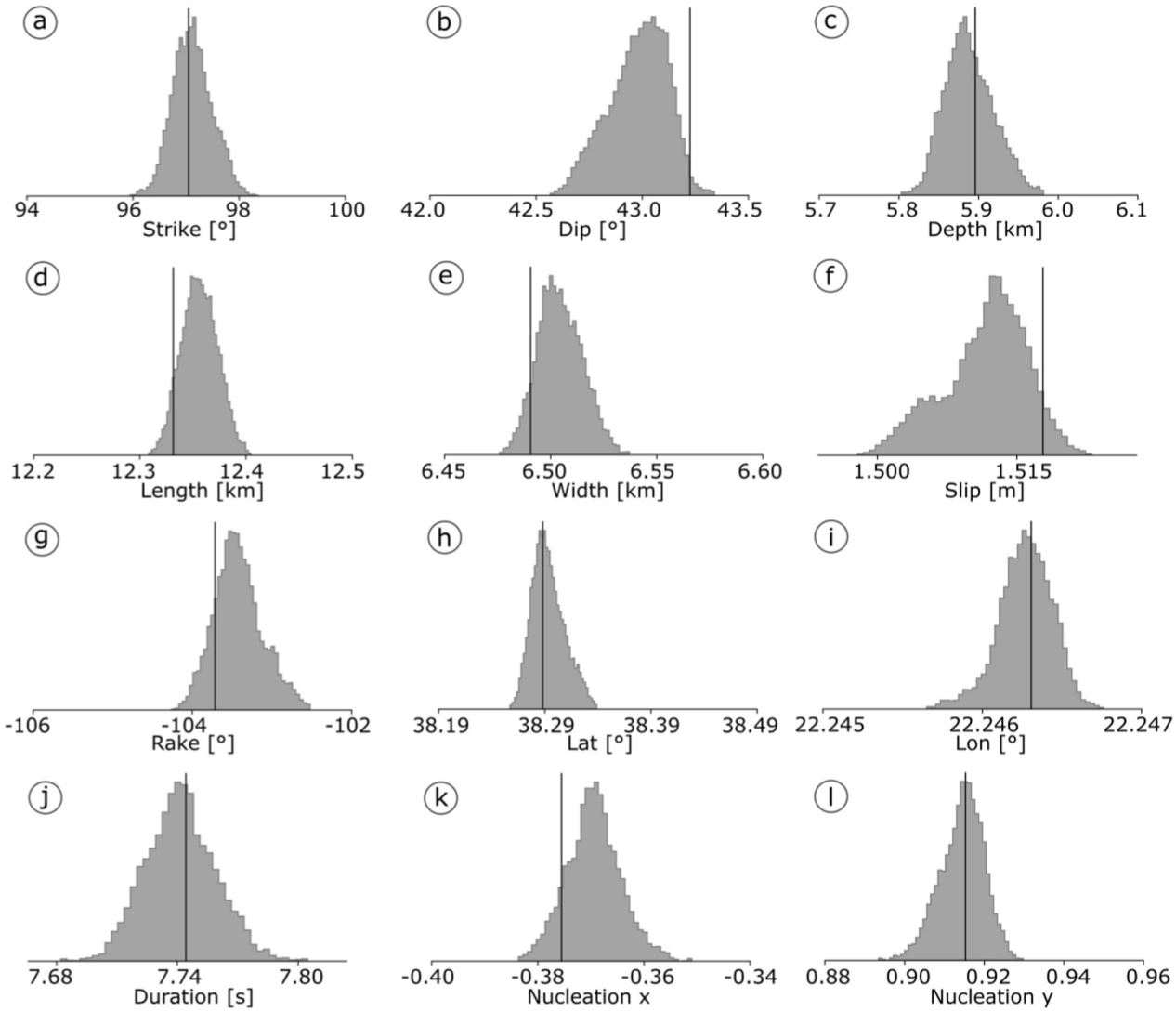

FIGURE 9
Distribution of the fault parameters for the joint inversion solution. **(a)** Strike in degrees; **(b)** dip angle in degrees; **(c)** depth in km; **(d)** length in km; **(e)** width in km; **(f)** slip in m; **(g)** rake in degrees; **(h)** latitude in degrees; **(i)** longitude in degrees; **(j)** duration in seconds; **(k)** nucleation for X direction (longitude); **(l)** nucleation in Y direction (latitude). Vertical black line represents the meta-model.

along both the Aigion and Eratini coasts. It is also reported in the literature that there was coastal slumping and liquefaction (Lekkas et al., 1998). The presence of minor ground fractures on part of the onshore Aigion fault, in conjunction with nearby coastal failure and liquefaction, does not provide unambiguous evidence to suggest that the Aigion fault is the primary source of the 1995 earthquake (McNeill et al., 2007; Pantosti et al., 2004). The aforementioned evidence thus also supports the possibility of the south-dipping fault source we present here.

The pattern of microseismicty also shows a dramatic change from west to east (Figure 1a). In the west, high rates of microseismicity have been recorded by the NOA catalogs during 1950–2008 (Makropoulos et al., 2012) and by the *Corinth Rift Laboratory* network since the early 2000s (Duverger et al., 2018; Cornet et al., 2004). High resolution relocation of the microseismicity suggests the majority of it aligns along a low angle north-dipping band, and possible detachment fault, at 5–10 km depth (Bernard et al., 2006), with the swarm-like nature of the seismicity being interpreted as potential fluid involvement helping aseismic deformation (Cornet et al., 2004). However, a key observation is that this zone of microseismicity terminates to the west of our modelled fault plane (Figure 10). On the other hand, the microseismicity of the region of our modelled fault rupture is low, scattered and difficult to define properly.

The presence and absence of microseismicity along different parts of the rift, as well as its characteristics, may be indicative of the state of kinematic locking on the associated normal faults. Specifically, the long-lived pattern of microseismicity in the western part of the rift is strong evidence that a significant amount of extension occurs by microseismic creep on faults, especially offshore (Bernard et al., 2006; see also Taupo Rift in New Zealand by Mouslopoulou et al., 2013). On the other hand, the lack of microseismicity near the position of our modelled fault rupture is best explained by dominant stick-slip

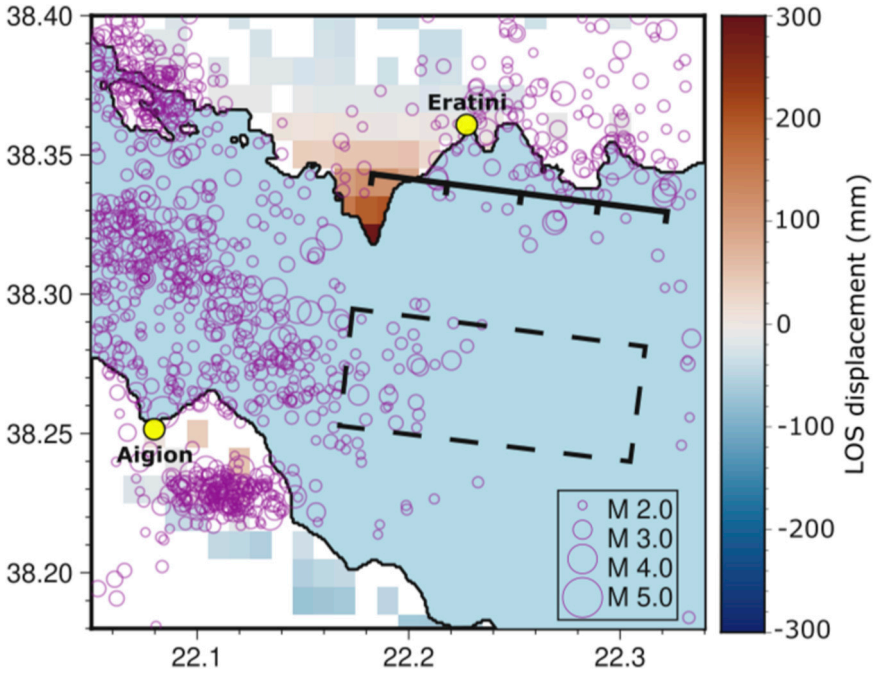

FIGURE 10
Offshore region of Aigion with the joint inversion solution and the microseismicity from 2012 to present day (National Observatory of Athens catalogue). The black line represents the fault at surface. The dashed rectangle represents the fault plane in depth. The purple cercles represents seismic events.

behaviour in this area. In this mode, the fault slips primarily during rapid slip and large magnitude earthquakes, before and after which the fault is locked (Byerlee, 1970). This has important implications for seismic hazard assessment since it implies that faults in the Corinth Rift that have been shown to be geological active during the Holocene but that lack microseismicity potentially deform mainly with classic co-seismic rupture followed by protracted elastic strain accumulation. Identifying locked faults that slip only during large magnitude co-seismic rupture has important implications for seismic hazard assessment. In contrast, faults creeping micro-seismically or asesimically are less likely to host large earthquakes.

Our modelling of the geodetic and seismological data can fit the observations with a single fault source, with the lack of residual signal suggesting insignificant slip on a second fault. Therefore, in our modelling, we prefer a simple one-fault model to a model including two or more faults. Furthermore, the earthquake sequence contains a single mainshock followed by aftershocks with smaller magnitudes not expected to cause measurable surface slip, suggesting dominant single fault slip. The solution proposed by our model suits the observed mainshock-aftershocks sequence and a more complex geometry is not justified by the observations. However, recent large earthquakes in Greece have shown the possibility of multi-fault rupture. For example, in central Greece the Tyrnavos sequence in March 2021 (M 5.7–6.3) ruptured 3 unrecognized normal faults (Chatzipetros et al., 2021; Ganas et al., 2021; Koukouvelas et al., 2021; Mouslopoulou et al., 2022). Another related example is the 1981 sequence in east Gulf of Corinth (M 6.4–6.7), triggering north- and south-dipping faults onshore and probably offshore, however this event involved multiple mainshocks (Jackson et al., 1982; Abercrombie et al., 1995). Multi-fault rupture may also occur through a single mainshock followed by aftershocks on adjacent faults, as observed during the 1987 M_w 6.5 Edgecumbe earthquake in New Zealand (Delano et al., 2022). If the 1995 sequence is a multi-fault rupture, our InSAR models imply that the secondary fault slip was negligible, an interpretation supported by the mainshock having M_w of 6.2, and the largest aftershock being in the range of M_w 5.2–5.6. We therefore infer that, during the 1995 sequence, the Aigion fault may have acted as a secondary structure but with minimal slip.

6 Conclusion

We study the M_w 6.2 Aigion earthquake that occurred in the Corinth Rift, Greece on 15 June 1995, using InSAR and seismic waveforms, since the subsurface geometry and position of the fault source is debated. This study also tests the appropriate method to evaluate offshore deformation. Three models were processed using the inversion method of elastic modelling of the ground motion to fully explore the range of fault models that explain the data. Firstly, by inversion of InSAR data only with two interferograms (ascending and descending) showing up to 24 cm of ground motion on the north coast, then joint inversion with seismic data (22 seismic stations). Joint inversion favours a south-dipping fault (43° dip) in contradiction to the fault geometry interpreted so far in the literature, striking east-west at 97° and coherent with the other normal faults of the rift and a realistic slip of 1.5 m (Figure 10). The earthquake source could be an extension of the south-dipping Trizonia fault on the north rift margin. Comparison of our modelled fault with microseismicity distribution suggests contrasting modes of slip in the rift, with some faults slipping continuously with microseismic creep, and others by stick-slip behaviour. The change

in fault slip behaviour along the rift (between microseismic creep and stick-slip) is coincident with the region of the 1995 earthquake. As the fault causing the Aigion earthquake was initially interpreted to be the Aigion fault or a nearby unmapped blind fault, but as our solution contradicts this with a south-dipping fault further north, it is important to reassess the seismic hazard of the region.

Data availability statement

The original contributions presented in the study are included in the article/Supplementary Material, further inquiries can be directed to the corresponding author.

Author contributions

MP: Methodology, Visualization, Writing – original draft, Writing – review and editing, Conceptualization, Investigation, Software. RV: Methodology, Software, Writing – review and editing, Formal Analysis. CP: Supervision, Validation, Writing – review and editing, Conceptualization. DK: Supervision, Validation, Writing – review and editing, Conceptualization. AL: Methodology, Software, Writing – review and editing. LM: Supervision, Writing – review and editing, Resources.

Funding

The author(s) declared that financial support was received for this work and/or its publication. The research is part of the PhD of M. Parnas under the XXXVIII PhD cycle of the University of Pisa in Geosciences and Environment. Marella Parnas thanks the Earth and Environment Institute of Strasbourg for hosting her internship and processing part of the modelling. Derek Keir and Lisa McNeill are partially supported through NERC grant UKRI277. Carolina Pagli and Alessandro La Rosa are supported by the SpaceItUp project funded by ASI and the Ministry of University and Research, MUR, under contract n. 2024–5-E.0 CUP n. I53D24000060005.

Conflict of interest

The author(s) declared that this work was conducted in the absence of any commercial or financial relationships that could be construed as a potential conflict of interest.

The author DK declared that they were an editorial board member of Frontiers at the time of submission. This had no impact on the peer review process and the final decision.

Generative AI statement

The author(s) declared that generative AI was not used in the creation of this manuscript.

Any alternative text (alt text) provided alongside figures in this article has been generated by Frontiers with the support of artificial intelligence and reasonable efforts have been made to ensure accuracy, including review by the authors wherever possible. If you identify any issues, please contact us.

Publisher's note

Supplementary material

The Supplementary Material for this article can be found online at: https://www.frontiersin.org/articles/10.3389/feart.2026.1702148/full#supplementary-material

SUPPLEMENTARY FIGURE S1
(left) Ascending and (right) descending wrapped interferogram from ERS satellite. One fringe goes from blue to red, approximately 7 fringes on the north coast can be counted on the ascending interferogram and approximately 9 on the north coast on the descending interferogram. No fringes are visible on the south coast on both interferograms. We note that the descending interferogram presents a better fringe pattern.

SUPPLEMENTARY FIGURE S2
(A) Ascending quad-tree and **(B)** descending quad-tree, obtain from the quadtree-partitioning algorithm used on the ascending and descending interferogram.

SUPPLEMENTARY FIGURE S3
All selected seismic stations for P (Z) and SH (T) waveforms. Black line represents the data; red line is the forward model. In the top right corner if each waveform, grey graph is the standard residual and orange graph is the variance reduction.

References

Abercrombie, R. E., Main, I. G., Douglas, A., and Burton, P. W. (1995). The nucleation and rupture process of the 1981 Gulf of Corinth earthquakes from deconvolved broad-band data. *Geophys. J. Int.* 120, 393–405. doi:10.1111/j.1365-246X.1995.tb01827.x

Armijo, R., Meyer, B., King, G. C. P., Rigo, A., and Papanastassiou, D. (1996). Quaternary evolution of the Corinth Rift and its implications for the late Cenozoic evolution of the Aegean. *Geophys. J. Int.* 126, 11–53. doi:10.1111/j.1365-246X.1996.tb05264.x

Athanasopoulou, E., Despoiniadou, V., Dritsos, S., Santini, A., and Moraci, N. (2008). The impact of earthquakes on the city of Aigio in Greece. Urban planning as a factor in mitigating seismic damage. *AIP Conf. Proc.* 1020, 1899–1907. doi:10.1063/1.2963826

Avallone, A., Briole, P., Agatza-Balodimou, A. M., Billiris, H., Charade, O., Mitsakaki, C., et al. (2004). Analysis of eleven years of deformation measured by GPS in the Corinth Rift Laboratory area. *Comptes Rendus. Geosci.* 336, 301–311. doi:10.1016/j.crte.2003.12.007

Bassin, C. (2000). The current limits of resolution for surface wave tomography in North America. *Eos Trans. AGU* 81, F897.

Beckers, A., Hubert-Ferrari, A., Beck, C., Bodeux, S., Tripsanas, E., Sakellariou, D., et al. (2015). Active faulting at the western tip of the Gulf of Corinth, Greece, from high-resolution seismic data. *Mar. Geol.* 360, 55–69. doi:10.1016/j.margeo.2014.12.003

Begg, J. G., Mouslopoulou, V., Heron, D., and Nicol, A. (2025). AFG - Active Faults Greece: a comprehensive geomorphology-based 1:25,000 fault database. *Sci. Data* 12, 1853. doi:10.1038/s41597-025-06283-z

Bell, R. E. (2008). *Tectonic evolution of the Corinth Rift (phd)*. Southampton, United Kingdom: University of Southampton.

Bell, R. E., McNeill, L. C., Bull, J. M., and Henstock, T. J. (2008). Evolution of the offshore western Gulf of Corinth. *Geol. Soc. Am. Bull.* 120, 156–178. doi:10.1130/B26212.1

Bell, R. E., McNeill, L. C., Bull, J. M., Henstock, T. J., Collier, R. E. L., and Leeder, M. R. (2009). Fault architecture, basin structure and evolution of the Gulf of Corinth Rift, central Greece. *Basin Res.* 21, 824–855. doi:10.1111/j.1365-2117.2009.00401.x

Bell, R. E., Duclaux, G., Nixon, C. W., Gawthorpe, R. L., and McNeill, L. C. (2018). High-angle, not low-angle, normal faults dominate early rift extension in the Corinth Rift, central Greece. *Geology* 46, 115–118. doi:10.1130/G39560.1

Bernard, P., Briole, P., Meyer, B., Lyon-Caen, H., Gomez, J.-M., Tiberi, C., et al. (1997). The Ms = 6.2, June 15, 1995 Aigion earthquake (Greece): evidence for low angle normal faulting in the Corinth rift. *J. Seismol.* 1, 131–150. doi:10.1023/A:1009795618839

Bernard, P., Boudin, F., Sacks, S., Linde, A., Blum, P.-A., Courteille, C., et al. (2004). Continuous strain and tilt monitoring on the Trizonia Island, Rift of Corinth, Greece. Comptes Rendus. *Géoscience* 336, 313–323. doi:10.1016/j.crte.2003.11.015

Bernard, P., Lyon-Caen, H., Briole, P., Deschamps, A., Boudin, F., Makropoulos, K., et al. (2006). Seismicity, deformation and seismic hazard in the western rift of Corinth: new insights from the Corinth Rift Laboratory (CRL). *Tectonophys. Nat. Laboratories Seismogenic Faults* 426, 7–30. doi:10.1016/j.tecto.2006.02.012

Briole, P., Rigo, A., Lyon-Caen, H., Ruegg, J. C., Papazissi, K., Mitsakaki, C., et al. (2000). Active deformation of the Corinth rift, Greece: results from repeated Global Positioning system surveys between 1990 and 1995. *J. Geophys. Res.* 105, 25605–25625. doi:10.1029/2000JB900148

Byerlee, J. D. (1970). The mechanics of stick-slip. *Tectonophysics* 9, 475–486. doi:10.1016/0040-1951(70)90059-4

Calais, E., Lesne, O., Déverchère, J., San'kov, V., Lukhnev, A. V., Miroshnichenko, A., et al. (1998). Crustal deformation in the Baikal rift from GPS measurements. *Geophys. Res. Lett.* 25, 4003–4006. doi:10.1029/1998GL900067

Cervelli, P., Murray, M. H., Segall, P., Aoki, Y., and Kato, T. (2001). Estimating source parameters from deformation data, with an application to the March 1997 earthquake swarm off the Izu Peninsula, Japan. *J. Geophys. Res. Solid Earth* 106, 11217–11237. doi:10.1029/2000JB900399

Chatzipetros, A., Pavlides, S., Foumelis, M., Sboras, S., Galanakis, D., Pikridas, C., et al. (2021). The northern Thessaly strong earthquakes of March 3 and 4, 2021, and their neotectonic setting. *Bull. Geol. Soc. Greece* 58, 222–255. doi:10.12681/bgsg.27225

Clarke, P. J., Davies, R. R., England, P. C., Parsons, B., Billiris, H., Paradissis, D., et al. (1998). Crustal strain in central Greece from repeated GPS measurements in the interval 1989–1997. *Geophys J. Int.* 135, 195–214. doi:10.1046/j.1365-246X.1998.00633.x

Clément, C., Sachpazi, M., Charvis, P., Graindorge, D., Laigle, M., Hirn, A., et al. (2004). Reflection–refraction seismics in the Gulf of Corinth: hints at deep structure and control of the deep marine basin. *Tectonophys. Act. Faulting Crustal Deformation East. Mediterr. Region* 391, 97–108. doi:10.1016/j.tecto.2004.07.010

Collier, R. E. L., Pantosti, D., D'Addezio, G., De Martini, P. M., Masana, E., and Sakellariou, D. (1998). Paleoseismicity of the 1981 Corinth earthquake fault: seismic contribution to extensional strain in central Greece and implications for seismic hazard. *J. Geophys. Res. Solid Earth* 103, 30001–30019. doi:10.1029/98JB02643

Cornet, F. H., Bernard, P., and Moretti, I. (2004). The corinth rift laboratory. Comptes rendus. *Géoscience* 336, 235–241. doi:10.1016/j.crte.2004.02.001

De Barros, L., Cappa, F., Deschamps, A., and Dublanchet, P. (2020). Imbricated aseismic slip and fluid diffusion drive a seismic swarm in the Corinth Gulf, Greece. *Geophys. Res. Lett.* 47, e2020GL087142. doi:10.1029/2020GL087142

De Martini, P. M., Pantosti, D., Palyvos, N., Lemeille, F., McNeill, L., and Collier, R. (2004). Slip rates of the Aigion and Eliki Faults from uplifted marine terraces, Corinth Gulf, Greece. *Comptes Rendus Geosci.* 336, 325–334. doi:10.1016/j.crte.2003.12.006

Del Moral, P., Doucet, A., and Jasra, A. (2006). Sequential monte carlo samplers. *J. R. Stat. Soc. Ser. B Stat. Methodol.* 68, 411–436. doi:10.1111/j.1467-9868.2006.00553.x

Delano, J. E., Howell, A., Stahl, T. A., and Clark, K. (2022). 3D coseismic surface displacements from historical aerial photographs of the 1987 edgecumbe earthquake, New Zealand. *J. Geophys. Res. Solid Earth* 127, e2022JB024059. doi:10.1029/2022JB024059

Duverger, C., Godano, M., Bernard, P., Lyon-Caen, H., and Lambotte, S. (2015). The 2003–2004 seismic swarm in the western Corinth rift: evidence for a multiscale pore pressure diffusion process along a permeable fault system. *Geophys. Res. Lett.* 42, 7374–7382. doi:10.1002/2015GL065298

Duverger, C., Lambotte, S., Bernard, P., Lyon-Caen, H., Deschamps, A., and Nercessian, A. (2018). Dynamics of microseismicity and its relationship with the active structures in the western Corinth Rift (Greece). *Geophys. J. Int.* 215, 196–221. doi:10.1093/gji/ggy264

Farr, T. G., Rosen, P. A., Caro, E., Crippen, R., Duren, R., Hensley, S., et al. (2007). The shuttle radar topography mission. *Rev. Geophys.* 45. doi:10.1029/2005RG000183

Ferretti, A., Monti-Guarnieri, A., Prati, C., Rocca, F., and Massonet, D. (2007). InSAR Principles - Guidelines for SAR interferometry processing and interpretation. *ESA Train. Man.* 19.

Ganas, A., Valkaniotis, S., Briole, P., Serpetsidaki, A., Kapetanidis, V., Karasante, I., et al. (2021). Domino-style earthquakes along blind normal faults in Northern Thessaly (Greece): kinematic evidence from field observations, seismology, SAR interferometry and GNSS. *Bull. Geol. Soc. Greece* 58, 37–86. doi:10.12681/bgsg.27102

Goldstein, R. M., and Werner, C. L. (1998). Radar interferogram filtering for geophysical applications. *Geophys. Res. Lett.* 25, 4035–4038. doi:10.1029/1998GL900033

Goldstein, R. M., Zebker, H. A., and Werner, C. L. (1988). Satellite radar interferometry: Two-dimensional phase unwrapping. *Radio Sci.* 23, 713–720. doi:10.1029/RS023i004p00713

Goldstein, R. M., Engelhardt, H., Kamb, B., and Frolich, R. M. (1993). Satellite radar interferometry for monitoring ice sheet motion: application to an antarctic ice stream. *Science* 262, 1525–1530. doi:10.1126/science.262.5139.1525

Hatzfeld, D., Karakostas, V., Ziazia, M., Kassaras, I., Papadimitriou, E., Makropoulos, K., et al. (2000). Microseismicity and faulting geometry in the Gulf of Corinth (Greece). *Geophys J. Int.* 141, 438–456. doi:10.1046/j.1365-246x.2000.00092.x

Jackson, J. A., Gagnepain, J., Houseman, G., King, G. C. P., Papadimitriou, P., Soufleris, C., et al. (1982). Seismicity, normal faulting, and the geomorphological development of the Gulf of Corinth (Greece): the Corinth earthquakes of February and March 1981. *Earth Planet. Sci. Lett.* 57, 377–397. doi:10.1016/0012-821X(82)90158-3

Jolivet, L., Labrousse, L., Agard, P., Lacombe, O., Bailly, V., Lecomte, E., et al. (2010). Rifting and shallow-dipping detachments, clues from the Corinth Rift and the Aegean. *Tectonophysics* 483, 287–304. doi:10.1016/j.tecto.2009.11.001

Jónsson, S., Zebker, H., Segall, P., and Amelung, F. (2002). Fault slip distribution of the 1999 Mw 7.1 hector mine, California, earthquake, estimated from satellite radar and GPS measurements. *Bull. Seismol. Soc. Am.* 92, 1377–1389. doi:10.1785/0120000922

Kapetanidis, V., Deschamps, A., Papadimitriou, P., Matrullo, E., Karakonstantis, A., Bozionelos, G., et al. (2015). The 2013 earthquake swarm in Helike, Greece: seismic activity at the root of old normal faults. *Geophys J. Int.* 202, 2044–2073. doi:10.1093/gji/ggv249

Kaviris, G., Elias, P., Kapetanidis, V., Serpetsidaki, A., Karakonstantis, A., Plicka, V., et al. (2021). The Western Gulf of Corinth (Greece) 2020–2021 seismic crisis and cascading events: first results from the corinth Rift laboratory network. *Seismic Rec.* 1, 85–95. doi:10.1785/0320210021

Kennett, B. L. N., Engdahl, E. R., and Buland, R. (1995). Constraints on seismic velocities in the Earth from traveltimes. *Geophys. J. Int.* 122, 108–124. doi:10.1111/j.1365-246X.1995.tb03540.x

Koukouvelas, I. K., and Doutsos, T. T. (1996). Implications of structural segmentation during earthquakes: the 1995 Egion earthquake, Gulf of Corinth, Greece. *J. Struct. Geol.* 18, 1381–1388. doi:10.1016/S0191-8141(96)00071-5

Koukouvelas, I. K., Stamatopoulos, L., Katsonopoulou, D., and Pavlides, S. (2001). A palaeoseismological and geoarchaeological investigation of the Eliki fault, Gulf of Corinth, Greece. *J. Struct. Geol.* 23, 531–543. doi:10.1016/S0191-8141(00)00124-3

Koukouvelas, I. K., Nikolakopoulos, K. G., Kyriou, A., Caputo, R., Belesis, A., Zygouri, V., et al. (2021). The March 2021 damasi earthquake sequence, Central Greece: reactivation evidence across the westward propagating tyrnavos Graben. *Geosciences* 11, 328. doi:10.3390/geosciences11080328

Lambotte, S., Lyon-Caen, H., Bernard, P., Deschamps, A., Patau, G., Nercessian, A., et al. (2014). Reassessment of the rifting process in the Western Corinth Rift from relocated seismicity. *Geophys. J. Int.* 197, 1822–1844. doi:10.1093/gji/ggu096

Lekidis, V. A., Karakostas, C. Z., Dimitriu, P. P., Margaris, B. N., Kalogeras, I., and Theodulidis, N. (1999). The aigio (greece) seismic sequence of June 1995: seismological, strong motion data and effects of the earthquakes on structures. *J. Earth. Eng.* 03, 349–380. doi:10.1142/S1363246999000156

Lekkas, E. L., Lozios, S. G., Skourtsos, E. N., and Kranis, H. D. (1998). Egio earthquake (15 June 1995): an episode in the neotectonic evolution of Corinthiakos Gulf. *J. Geodyn.* 26, 487–499. doi:10.1016/S0264-3707(97)00073-2

Lyon-Caen, H., Papadimitriou, P., Deschamps, A., Bernard, P., Makropoulos, K., Pacchiani, F., et al. (2004). First results of the CRLN seismic network in the western Corinth Rift: evidence for old-fault reactivation. *Comptes Rendus. Géoscience* 336, 343–351. doi:10.1016/j.crte.2003.12.004

Makropoulos, K., Kaviris, G., and Kouskouna, V. (2012). An updated and extended earthquake catalogue for Greece and adjacent areas since 1900. *Nat. Hazards Earth Syst. Sci.* 12, 1425–1430. doi:10.5194/nhess-12-1425-2012

Massonnet, D., Rossi, M., Carmona, C., Adragna, F., Peltzer, G., Feigl, K., et al. (1993). The displacement field of the Landers earthquake mapped by radar interferometry. *Nature* 364, 138–142. doi:10.1038/364138a0

Mats, V. D. (1993). The structure and development of the Baikal rift depression. *Earth-Science Rev.* 34, 81–118. doi:10.1016/0012-8252(93)90028-6

McKenzie, D. (1972). Active tectonics of the Mediterranean Region. *Geophys J. Int.* 30, 109–185. doi:10.1111/j.1365-246X.1972.tb02351.x

McKenzie, D. (1978). Active tectonics of the Alpine—himalayan belt: the Aegean Sea and surrounding regions. *Geophys J. Int.* 55, 217–254. doi:10.1111/j.1365-246X.1978.tb04759.x

McNeill, L. C., Cotterill, C. J., Henstock, T. J., Bull, J. M., Stefatos, A., Collier, R. E. Ll., et al. (2005a). Active faulting within the offshore western Gulf of Corinth, Greece: implications for models of continental rift deformation. *Geology* 33, 241–244. doi:10.1130/G21127.1

McNeill, L. C., Collier, R. E. Ll., De Martini, P. M., Pantosti, D., and D'Addezio, G. (2005b). Recent history of the Eastern Eliki Fault, Gulf of Corinth: geomorphology, palaeoseismology and impact on palaeoenvironments. *Geophys J. Int.* 161, 154–166. doi:10.1111/j.1365-246X.2005.02559.x

McNeill, L. C., Cotterill, C. J., Bull, J. M., Henstock, T. J., Bell, R., and Stefatos, A. (2007). Geometry and slip rate of the Aigion fault, a young normal fault system in the western Gulf of Corinth. *Geol* 35, 355. doi:10.1130/G23281A.1

Melgar, D., Ganas, A., Geng, J., Liang, C., Fielding, E. J., and Kassaras, I. (2017). Source characteristics of the 2015 Mw6.5 Lefkada, Greece, strike-slip earthquake. *J. Geophys. Res. Solid Earth* 122, 2260–2273. doi:10.1002/2016JB013452

Mouslopoulou, V., Hristopulos, D. T., Nicol, A., Walsh, J. J., and Bannister, S. (2013). The importance of microearthquakes in crustal extension of an active rift: a case study from New Zealand. *J. Geophys. Res. Solid Earth* 118, 1556–1568. doi:10.1002/jgrb.50062

Mouslopoulou, V., Sudhaus, H., Konstantinou, K. I., Begg, J., Saltogianni, V., Männel, B., et al. (2022). A deeper look into the 2021 Tyrnavos Earthquake Sequence (TES) reveals coseismic breaching of an unrecognized large-scale fault relay Zone in Continental Greece. *Tectonics* 41, e2022TC007453. doi:10.1029/2022TC007453

Mouslopoulou, V., Begg, J. G., Polonia, A., Nicol, A., Reston, T. J., Cesca, S., et al. (2025). Hellenic subduction System and upper-plate structures revealed by deep high-resolution seismic-reflection profiles and seafloor bathymetry. *Tectonics* 44, e2025TC008943. doi:10.1029/2025TC008943

Mustać, M., Hejrani, B., Tkalčić, H., Kim, S., Lee, S., and Cho, C. (2020). Large isotropic component in the source mechanism of the 2013 democratic People's Republic of Korea nuclear test revealed via a hierarchical bayesian inversion. *Bull. Seismol. Soc. Am.* 110, 166–177. doi:10.1785/0120190062

Nikolopoulou, I., Sokos, E., Roumelioti, Z., and Mouslopoulou, V. (2025). Seismotectonics of the gulf of Patras, Central Greece: new insights from earthquake relocation, focal mechanisms and stress inversion. *Tectonophysics* 913, 230889. doi:10.1016/j.tecto.2025.230889

Nixon, C. W., McNeill, L. C., Bull, J. M., Bell, R. E., Gawthorpe, R. L., Henstock, T. J., et al. (2016). Rapid spatiotemporal variations in rift structure during development of the Corinth Rift, central Greece. *Tectonics* 35, 1225–1248. doi:10.1002/2015TC004026

Nixon, C. W., McNeill, L. C., Gawthorpe, R. L., Shillington, D. J., Michas, G., Bell, R. E., et al. (2024). Increasing fault slip rates within the Corinth Rift, Greece: a rapidly localising active rift fault network. *Earth Planet. Sci. Lett.* 636, 118716. doi:10.1016/j.epsl.2024.118716

Okada, Y. (1985). Surface deformation due to shear and tensile faults in a half-space. *Bull. Seismol. Soc. Am.* 75, 1135–1154. doi:10.1785/BSSA0750041135

Omar, G. I., and Steckler, M. S. (1996). Fission track evidence on the initial rifting of the Red Sea: two pulses, no propagation. *Oceanogr. Lit. Rev.* 7, 684–1344. doi:10.1126/science.270.5240.1341

Palyvos, N., Pantosti, D., De Martini, P. M., Lemeille, F., Sorel, D., and Pavlopoulos, K. (2005). The Aigion–Neos Erineos coastal normal fault system (western Corinth Gulf Rift, Greece): geomorphological signature, recent earthquake history, and evolution. *J. Geophys. Res. Solid Earth* 110. doi:10.1029/2004JB003165

Pantosti, D., De Martini, P. M., Koukouvelas, I., Stamatopoulos, L., Palyvos, N., Pucci, S., et al. (2004). Palaeoseismological investigations of the Aigion Fault (Gulf of Corinth, Greece). *Comptes Rendus Geosci.* 336, 335–342. doi:10.1016/j.crte.2003.12.005

Papadopoulos, G. A., Agalos, A., Karavias, A., Triantafyllou, I., Parcharidis, I., and Lekkas, E. (2021). Seismic and geodetic imaging (DInSAR) investigation of the March 2021 strong earthquake sequence in Thessaly, Central Greece. *Geosciences* 11, 311. doi:10.3390/geosciences11080311

Peacock, D. C. P., and Sanderson, D. J. (1994). Geometry and development of relay ramps in normal fault systems. *AAPG Bull.* 78, 147–165. doi:10.1306/BDFF9046-1718-11D7-8645000102C1865D

Pichon, X. L., and Angelier, J. (1979). The hellenic arc and trench system: a key to the neotectonic evolution of the eastern mediterranean area. *Tectonophysics* 60, 1–42. doi:10.1016/0040-1951(79)90131-8

Rigo, A., Lyon-Caen, H., Armijo, R., Deschamps, A., Hatzfeld, D., Makropoulos, K., et al. (1996). A microseismic study in the western part of the Gulf of Corinth (Greece): implications for large-scale normal faulting mechanisms. *Geophys. J. Int.* 126, 663–688. doi:10.1111/j.1365-246X.1996.tb04697.x

Rosen, P. A., Gurrola, E., Sacco, G. F., and Zebker, H. (2012). "The InSAR scientific computing environment," in *EUSAR 2012; 9th European Conference on Synthetic Aperture Radar. Presented at the EUSAR 2012; 9th European Conference on Synthetic Aperture Radar*, 730–733.

Saria, E., Calais, E., Stamps, D. S., Delvaux, D., and Hartnady, C. J. H. (2014). Present-day kinematics of the East African Rift. *J. Geophys. Res. Solid Earth* 119, 3584–3600. doi:10.1002/2013JB010901

Schmidt, J. F. J. (1879). Studien über erdbeben. A. Georgi.

Sigmundsson, F. (2018). Chapter 11 - magma movements in volcanic plumbing systems and their associated ground deformation and seismic patterns.

Singh, T., Nain, N., Monterroso, F., Caputo, R., Striano, P., Yadav, R. B. S., et al. (2025). The Afghanistan earthquake of 21 June 2022: the role of compressional step-overs in seismogenesis. *Geosciences* 15, 156. doi:10.3390/geosciences15040156

Sokos, E., Zahradník, J., Kiratzi, A., Janský, J., Gallovič, F., Novotny, O., et al. (2012). The January 2010 Efpalio earthquake sequence in the western Corinth Gulf (Greece). *Tectonophysics* 530–531, 299–309. doi:10.1016/j.tecto.2012.01.005

Sokos, E., Zahradník, J., Gallovič, F., Serpetsidaki, A., Plicka, V., and Kiratzi, A. (2016). Asperity break after 12 years: the Mw6.4 2015 Lefkada (Greece) earthquake. *Geophys. Res. Lett.* 43, 6137–6145. doi:10.1002/2016GL069427

Stavropoulos, A. (1954). *The history of the town of Egio*. Athens (In Greek), 699.

Stein, A. M. (1988). Basement controls upon basin development in the Caledonian foreland, NW Scotland. *Basin Res.* 1, 107–119. doi:10.1111/j.1365-2117.1988.tb00008.x

Stein, R. S., and Barrientos, S. E. (1985). Planar high-angle faulting in the basin and range: geodetic analysis of the 1983 Borah Peak, Idaho, earthquake. *J. Geophys. Res.* 90, 11355–11366. doi:10.1029/JB090iB13p11355

Steinberg, A., Sudhaus, H., Heimann, S., and Krüger, F. (2020). Sensitivity of InSAR and teleseismic observations to earthquake rupture segmentation. *Geophys. J. Int.* 223, 875–907. doi:10.1093/gji/ggaa351

Stiros, S. C. (2021). The 373 B.C. helike (Gulf of corinth, Greece) earthquake and tsunami, revisited. *Seismol. Res. Lett.* 93, 444–457. doi:10.1785/0220210092

Taylor, B., Weiss, J. R., Goodliffe, A. M., Sachpazi, M., Laigle, M., and Hirn, A. (2011). The structures, stratigraphy and evolution of the Gulf of Corinth rift, Greece. *Geophys. J. Int.* 185, 1189–1219. doi:10.1111/j.1365-246X.2011.05014.x

Taymaz, T., Jackson, J., and Westaway, R. (1990). Earthquake mechanisms in the Hellenic Trench near Crete. *Geophys J. Int.* 102, 695–731. doi:10.1111/j.1365-246X.1990.tb04590.x

Taymaz, T., Jackson, J., and McKenzie, D. (1991). Active tectonics of the north and central Aegean Sea. *Geophys. J. Int.* 106, 433–490. doi:10.1111/j.1365-246X.1991.tb03906.x

Taymaz, T., Westaway, R., and Reilinger, R. (2004). Active faulting and crustal deformation in the Eastern Mediterranean region. *Tectonophys. Act. Faulting Crustal Deformation East. Mediterr. Region* 391, 1–9. doi:10.1016/j.tecto.2004.07.005

Taymaz, T., Yilmaz, Y., and Dilek, Y. (2007). *The Geodynamics of the Aegean and Anatolia: introduction*. London, United Kingdom: Geological Society, 291, 1–16. doi:10.1144/SP291.1

Vaka, D. S., Rao, Y. S., and Singh, T. (2020). "Surface deformation of the 2019 mirpur earthquake estimated from Sentinel-1 Insar Data," in *2020 IEEE India Geoscience and Remote Sensing Symposium (InGARSS)*. Presented at the 2020 IEEE India Geoscience and Remote Sensing Symposium (InGARSS), 130–133. doi:10.1109/InGARSS48198.2020.9358915

Vasyura-Bathke, H., Dettmer, J., Steinberg, A., Heimann, S., Isken, M., Zielke, O., et al. (2019). BEAT - Bayesian earthquake analysis tool. doi:10.5880/FIDGEO.2019.024

Vasyura-Bathke, H., Dettmer, J., Steinberg, A., Heimann, S., Isken, M. P., Zielke, O., et al. (2020). The bayesian earthquake analysis tool. *Seismol. Res. Lett.* 91, 1003–1018. doi:10.1785/0220190075

Viltres, R., Nobile, A., Vasyura-Bathke, H., Trippanera, D., Xu, W., and Jónsson, S. (2021). Transtensional rupture within a Diffuse Plate boundary Zone during the 2020 Mw 6.4 Puerto Rico Earthquake. *Seismol. Res. Lett.* 93, 567–583. doi:10.1785/0220210261

Wang, R., Lorenzo-Martín, F., and Roth, F. (2006). PSGRN/PSCMP—a new code for calculating co- and post-seismic deformation, geoid and gravity changes based on the viscoelastic-gravitational dislocation theory. *Comput. and Geosciences* 32, 527–541. doi:10.1016/j.cageo.2005.08.006

Wang, R., Yang, Z., Liu, L., Deng, J., and Chen, F. (2014). Decoupling noise and features *via* weighted ℓ1-analysis compressed sensing. *ACM Trans. Graph.* 33 (18), 1–18. doi:10.1145/2557449

Wells, D. L., and Coppersmith, K. J. (1994). New empirical relationships among magnitude, rupture length, rupture width, rupture area, and surface displacement. *Bull. Seismological Soc. Am.* 84, 974–1002. doi:10.1785/BSSA0840040974

Welstead, S. T. (1999). *Fractal and wavelet image compression techniques*. Bellingham, WA: SPIE Press.

Wright, T. J., Maghsoudi, Y., Lazecky, M., Hooper, A. J., Elliott, J. R., Ou, Q., et al. (2023). From Türkiye to China: tectonic strains and velocities in the Alpine-Himalayan Belt from Sentinel-1 InSAR and GNSS. *Present. A. T. AGU Fall Meet. Abstr.* G31A.

Yolsal-Çevikbilen, S., Taymaz, T., and Helvacı, C. (2014). Earthquake mechanisms in the Gulfs of Gökova, Sığacık, Kuşadası, and the Simav Region (western Turkey): neotectonics, seismotectonics and geodynamic implications. *Tectonophys. Cenozoic Extensional Tect. West. Central Anatolia, Turk.* 635, 100–124. doi:10.1016/j.tecto.2014.05.001